Chapter 2

Experimental Apparatus and Measurement Techniques

In this chapter, a description of the apparatus and measurement techniques used during this work will be presented. The majority of experiments made in this thesis were performed with photo-electron and photo-ion time-of-flight (TOF) spectroscopy of gas phase C_{60} after interaction with femtosecond laser pulses. A description of the experiments will be made starting from production of the molecular beam, then the excitation sources, and finally detection of the ions or electrons produced in the laser-matter interaction. The emphasis will be on experimental considerations which are important for the interpretation of the results. Additionally, instruments that were used during collaborations with other groups and which provided key results relating to this work will be briefly described.

2.1 Vacuum Chamber

The experiments were performed in a vacuum chamber. A photograph of the vacuum apparatus and the schematic of the experiment are shown in Fig. 2.1 and Fig. 2.2, respectively. The molecular beam, laser beam, and TOF axes are all oriented perpendicular to each other. Three turbo molecular pumps were used to evacuate the chamber. The interaction region, as well as the drift tubes had a background pressure on the order of 10^{-7} Torr. Background gases include water, acetone (the usual cleaning agent used), and Xenon (used for calibration of the photoelectron spectrometer). The ion signals due to these species can clearly be distinguished in the mass spectra from the masses of interest. A low pressure ($< 10^{-6}$ Torr) is needed for electron
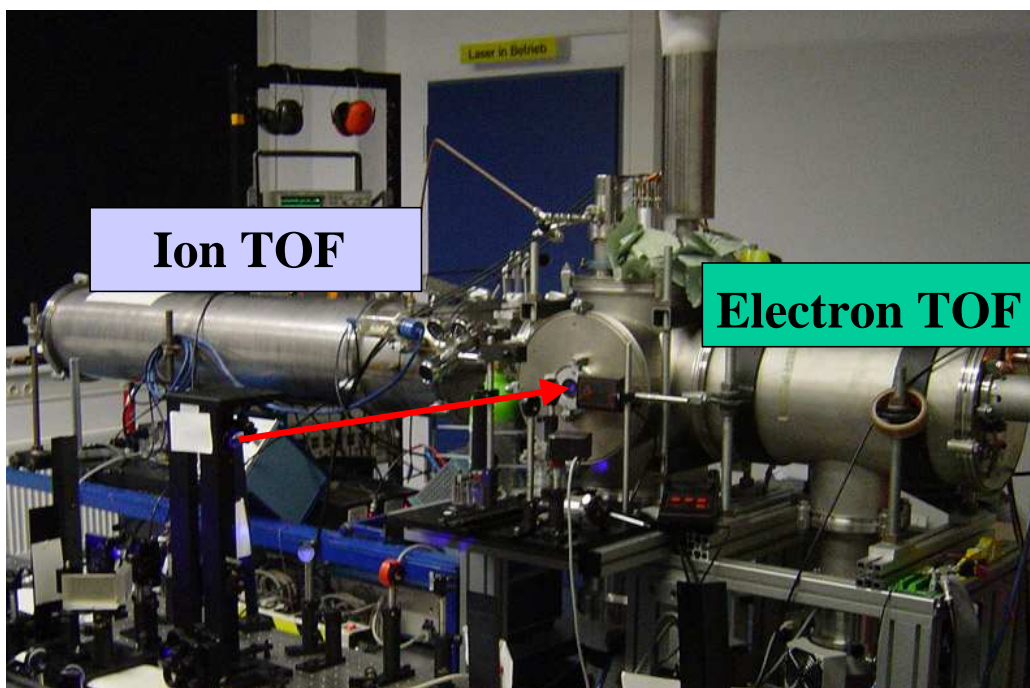
Figure 2.1: *Photograph of Apparatus setup at the Clark System April 2003. The ion TOF, electron TOF, and laser beam are indicated.*
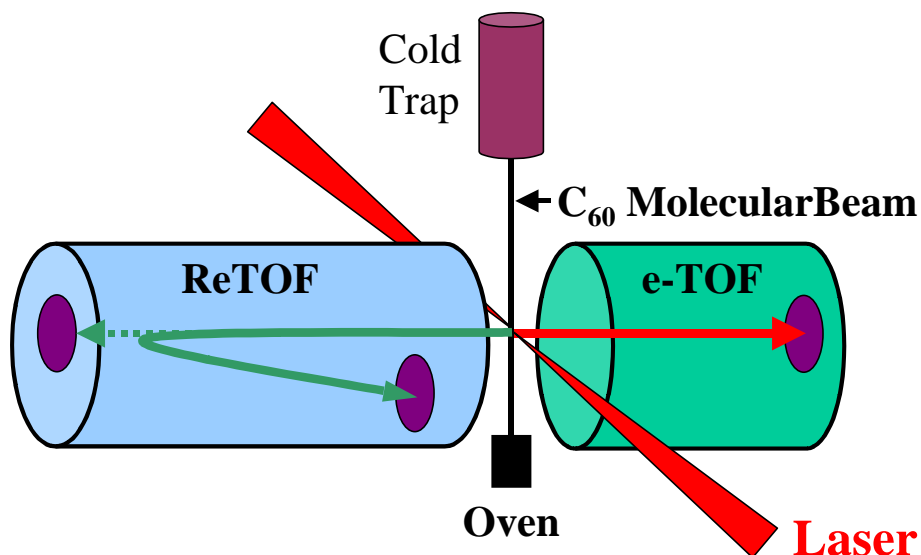

Figure 2.2: *Schematic of the experimental apparatus. The three axes, the laser beam, the molecular beam, and the time of flight, are perpendicular to each other. The ions are accelerated through either a linear or reflectron time of flight apparatus, while the electrons are collected in a linear time of flight without extraction.*

detection, where the ability to distinguish the source of the electrons was (for this apparatus) not possible.

The pressure of the chamber was not affected by the molecular beam. A cold plate was placed above the interaction region to reduce the amount of reflected C$_{60}$ as well as small particles, since they would lose kinetic energy (or even stick) upon collision with the cold plate. The pressure can be improved slightly ($\sim 0.5*10^{-7}$ Torr) when liquid nitrogen was used to cool the plate.

2.2 C$_{60}$ Molecular Beam

2.2.1 Effusive Molecular Beam Oven Source

A continuous effusive C$_{60}$ molecular beam is generated by a resistively heated oven with a knife-edge orifice of 1 mm diameter. An effusive beam is produced under the following conditions : a.) the thickness of the aperture is negligible in comparison to the mean free path b.) the spatial and velocity distributions of the molecules inside the source are not affected by the effusion [Ram56].

The mean free path can be calculated by Eq. 2.1,

$$\lambda = \frac{1}{n\sigma\sqrt{2}} \tag{2.1}$$

where n is the density of particles given by $P = nkT$, with P is the pressure, k is the Boltzmann constant and T is temperature, and σ is the cross section in units of Å^2. Using the vapor pressure of C$_{60}$ at 500°C [JKa00], and the geometric cross section, the mean free path is 7.27 mm. This is greater (but not considerably greater) than the aperture dimensions. The true angular and velocity distribution for this oven has not been measured. However, assuming nearly effusive emission, a reasonable approximation of the density of particles in the interaction region can be calculated.

An effusive beam emits in a 2π solid angle (forward direction) from an orifice. A 1 mm diameter aperture placed 1 cm away from the oven orifice was used to collimate the effusive molecular beam in the interaction region. The aperture is 4 cm from the interaction region. The right hand side of Fig. 2.3 displays a schematic picture (not to scale) of the experimental apparatus with the important distances noted.
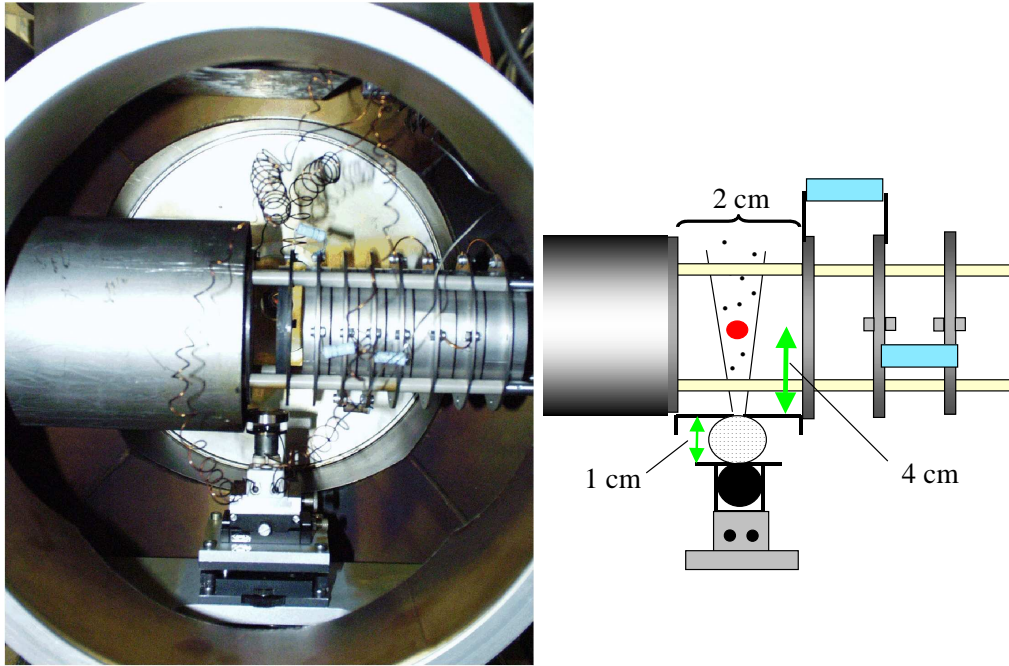
Figure 2.3: *The left side of the figure contains a photograph of the oven and acceleration region. The right hand side shows a schematic of the apparatus. The large dot in the center of the molecular beam represents the laser beam that propagates perpendicular to the page. At a distance of 1 cm from the oven orifice is an aperture of 1 mm diameter.*

The large circle in the molecular beam represents the laser beam, which propagates perpendicular to the page.

The typical spot size of the laser (μm^2) is much smaller than the width of the molecular beam (mm). The density of particles can be estimated from the distance from the effusive oven source to the interaction region. The density of particles, n_r, in the interaction region can be calculated by Eq. 2.13 [Ram56].

$$n_r = \frac{1}{3}\frac{A_s n_0}{\pi^{3/2} r^2} \tag{2.2}$$

where A_s is the cross-sectional area of the oven orifice, r is the distance from the oven opening, and $n_0 = p_0/kT_0$.

The initial temperature was typically set to 500°C $\pm$ 15°C, however the temperature during the experiments would fluctuate by 3°C (assuming a constant power on the oven). The vapor pressure of C_{60} at 500°C is 0.066 Pa [AOB92, SFH00]. This results in a particle density of $1.8*10^8$ particles/cm^3. The density of particles is exponentially dependent on the temperature, as is shown in Fig. 2.4. In the plot, two

boxes are drawn to indicate the change of density due to temperature fluctuations in setting the temperature (larger box) or during a measurement (smaller box). A closer look at the particle density, shows that a 3°C variation in temperature results in a change in density of 1.42×10^8 to 1.87×10^8 cm^3, or approximately 25%. The fluctuation of 3°C typically occurred over the course of several hours.   The fluctuation
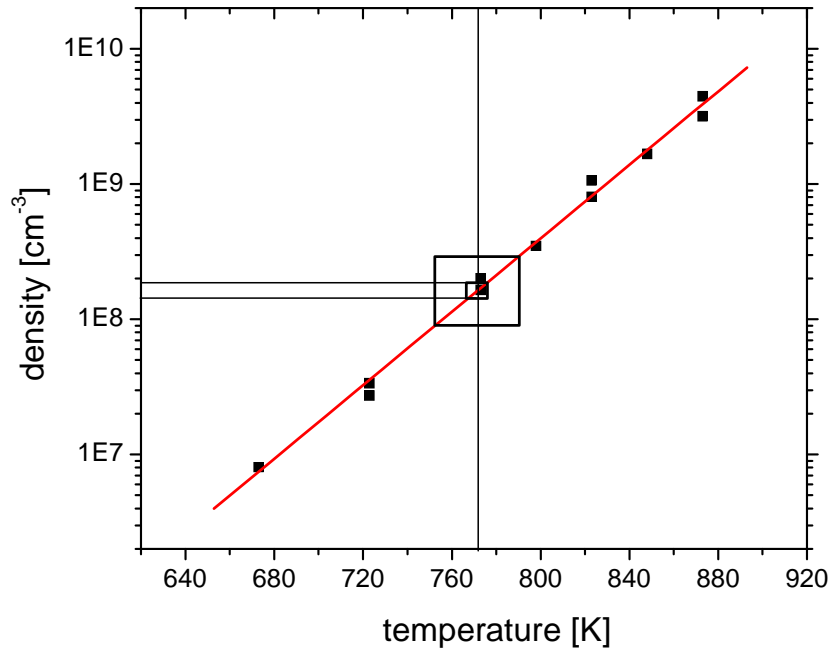

Figure 2.4: *Density as a function of temperature (values from [AOB92]). The vertical line indicates the most often used temperature of 770 K. The larger box indicates the range of experimental values, while the small box indicates the range of temperature fluctuation over several hours.*

of temperature is important to consider for experiments which are recorded over the course of several hours, for example, optimization loops which make a quantitative comparison of yields. The influence of temperature on the yield of ions will be further considered in Chapter 6.

The velocity distribution is broad due to the effusive nature of the molecular beam and can be described by a Maxwell-Boltzmann distribution. After the knife edge slit, the molecular beam is nearly unidirectional (within a few percent), thus only the scalar quantity, speed, needs to be considered. A Maxwellian speed distribution is given by Eq. 2.3.

$$f(v)dv = 4\pi(\frac{m}{2\pi kT})^{3/2}v^2 e^{-\frac{mv^2}{2kT}} \qquad (2.3)$$

where m is the mass of the particle, k is Boltzmann's constant, T is the temperature, and v is the velocity. The average speed is given by

$$\langle v \rangle = \sqrt{\frac{8kT}{\pi m}} \qquad (2.4)$$

For C_{60} at 420°C, the average speed is 143 m/s. In 100 ps, the longest pump-probe delay used in this work, C_{60} moves about 15 nm, which is much smaller than the focal spot size. In 50μs, the time-of-flight for C_{60} in the linear TOF apparatus, it will "drift" 7.5 mm, which is significantly smaller than the MCP detector size.

The distribution of C_{60}^+ particles along the molecular beam propagation axis is shown in Fig. 2.5. The left hand side plots the spatial distribution as measured with a position sensitive detector (Roentdek) (see Fig. 2.22 for apparatus geometry). The operation and characterization of this detector will be described in detail later in Section 2.6. Here, it is sufficient to know that there is a direct conversion between pixels and velocity.

The size and shape of the distribution of C_{60}^+ on the position sensitive detector, provides information about the experimental geometry of the apparatus. The laser beam propagates along the x-axis while the molecular beam propagates along the y-axis, as indicated by the two arrows.

The spatial distribution is elongated along the molecular beam axis and can be explained through consideration of the Maxwellian speed distribution of C_{60} particle emitted from the effusive oven source. The right-hand side of Fig. 2.5 shows the projection of a slice of 5 pixels from the center of the distribution of the 2-D image in addition to a Maxwell speed distribution and a Gaussian distribution. The best fit of the experimental data is with a Maxwellian speed distribution corresponding to a temperature of 420°C ± 20°C, which matches, within error, the experimentally measured temperature of 415°C. The zero velocity along the y-axis has been fixed with the fit of the Maxwellian distribution. Experimentally this occurs near the bottom of the 2D projection.

The x-projection can be reasonably fit by a Gaussian as seen in Fig. 2.6. The width of the Gaussian fit at FWHM = 109.3 ± 0.4 m/s. This corresponds to a width of 4.1 mm. This projection is more difficult to interpret since the width results from a convolution of the laser beam focus with the divergence of the molecular beam.
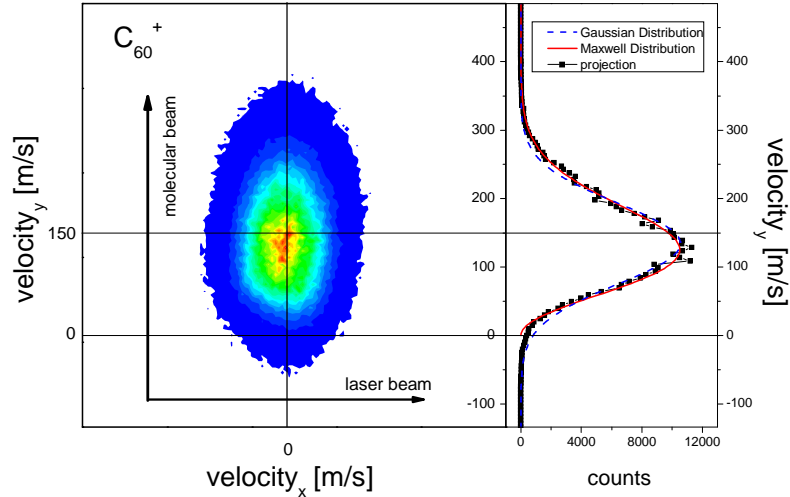
Figure 2.5: *Maxwell speed distribution of the C$_{60}$ molecular beam. Left: spatial distribution of C$_{60}^+$ measured with Roentdek position sensitive detector. Right: projection of a thin slice of spatial distribution and Maxwell speed distribution fit. The best fit was with a temperature of 420° C, which is comparable to the measured oven temperature of 415° C.*
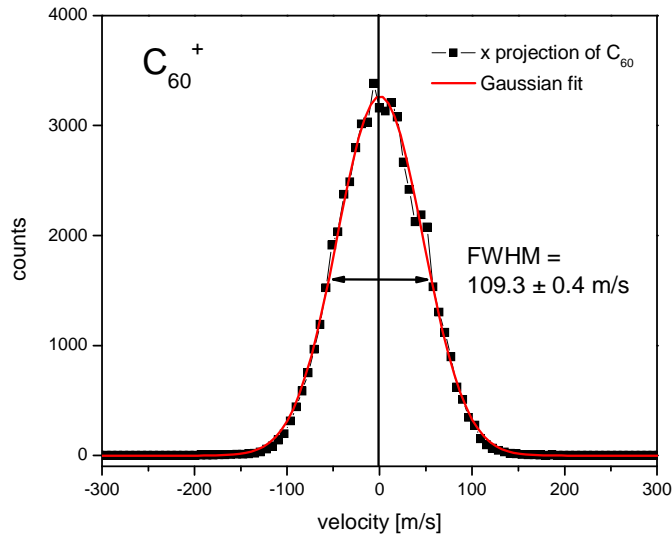

Figure 2.6: *A look at the x projection of the spatial distribution measured with a position sensitive detector. The projection is a thin slice of 5 pixels from the center of the distribution. The FWHM width of the Gaussian fit is 109.3 m/s, which corresponds to a length of 4.1 mm. Zero velocity is defined at the center of the Gaussian.*

Using an average velocity of 143 m/s found in Fig. 2.5, the lateral FWHM velocity corresponds to a beam divergence of $\sim \pm\frac{FWHM}{2*143} = 0.38$ rad or 22 degrees, which is larger than would be derived from the geometry indicated in Fig. 2.3.

An important factor to determine the width is the possibility of fragmentation after the acceleration. The kinetic energy release associated with the fragmentation process will increase the measured width. The interpretation of the widths will be further considered in Chapter 5.

The internal temperature has another important consequence for the interpretation of the results presented in this work. The C_{60} molecules iminating in thermal equilibrium, and considering the 3n - 6 = 174 vibrational degrees of freedom, the C_{60} molecule contains approximately 4.4 eV of internal energy before excitation with the femtosecond laser pulses. This can be calculated using the Eq. 2.5 [RWK01],

$$E_{in} = \frac{(3\widetilde{n} - 6)h\nu}{exp[h\nu/k_B T] - 1} \tag{2.5}$$

where $\widetilde{n}$ is the number of atoms in the fullerene and the average vibrational energy, ν, was taken to be that of the neutral system, i.e., 2.7×10^{13} Hz. The 4.4 eV is still small in comparison to the fragmentation threshold of C_{60} of 40 eV [HCF94].

2.2.2   Cold Molecular Beam Source

The internal temperature of C_{60} resulting from the effusive oven is 4.4 eV (see section about the oven). This energy is stored in vibrations which could mediate the absorption of energy. Therefore, a "Cold Source" apparatus, providing a molecular beam of C_{60} with a temperature of ~ 80 K [HMH97, HHM96, HMB97], was brought to Berlin in a collaboration with the group of Prof. E.E.B. Campbell. An estimation of the population of vibrational levels at 80 K shows that nearly all molecules from the cold source remains in the ground vibrational level, with as little as 0.6 percent in the first excited state.

The source is similar to the cluster aggregation type sources used in the groups of Martin [ZMN94] and Haberland [ESS95]. The cold molecular beam is generated in an aggregation cell with liquid nitrogen cooled walls and filled with a helium buffer gas, as is shown in Fig. 2.7. A resistively heated oven sublimes C_{60} into the gas phase, which then has ample time for collisional cooling with helium, reducing the internal temperature.

The cold source was directly attached to the time-of-flight apparatus shown in Fig. 2.13, and the same extraction meshes and fields were used as for the linear or reflectron time-of-flight. Due to the high velocity of the C_{60} molecules in the cold molecular beams, deflection plates were introduced into the apparatus. These will be discussed in Section 2.5.

If the density of C_{60} is large enough, which is controlled by the oven temperature, clusters of C_{60} can form, as is seen in Fig. 2.8. The excitation source used in this case was a 100 fs, 800 nm Ti:Sapphire with a fluence of 1 J/cm^2. The broad peaks near masses of C_{120}^+ and C_{180}^+ indicate the formation of clusters of C_{60}. The substructure is a series of peaks separated by C_2 units. This fragmentation pattern may be explained by coalescence of the fullerene cluster [YHD93], followed by C_2 loss. If the temperature of the oven is low enough, i.e., at low density of molecules, clustering is no longer favorable, which ensures that only cold, isolated C_{60} is present in the interaction region. All photoelectron spectra taken with the cold source and presented in this thesis were taken in the regime where no clusters were formed, i.e., ≤ 470 °C.

2.3 Femtosecond Irradiation Sources

The primary sources of laser radiation used in this work to excite fullerenes are amplified Ti:Sapphire Laser systems. At the Max Born Institute, one has the capability of using various laser sources. The source is selected depending on the experimental question to be answered. The majority of results presented in this work used either the fundamental wavelength (800 nm) or the second harmonic (400 nm) generated in a second harmonic generation (SHG) crystal.

The basis of every system is a femtosecond Ti:sapphire oscillator. The output energy per pulse of these lasers are in the nano-Joule region, which is far too weak for the multiple photon excitation and ionization needed for C_{60}. Thus, the pulses need to be further amplified.

Each of these systems use chirped pulse amplification (CPA) to provide high power yet short pulse duration. CPAs circumvent nonlinear effects and damage thresholds by stretching the incoming, oscillator pulse in time and thus reducing intensity. After the pulse has been amplified, the pulse is temporally compressed.

The majority of these systems are regenerative amplification systems. Regenerative amplification seeds one of the stretched oscillator pulses into a cavity where it
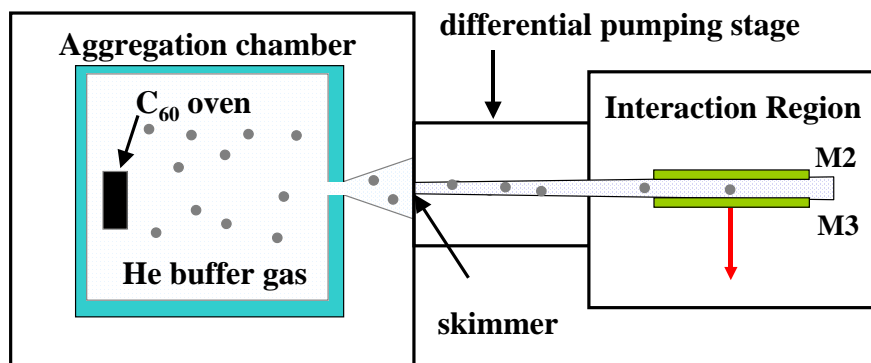
Figure 2.7: *Schematic of Cold source apparatus. The C_{60} is sublimated with a resistively heated oven, which lies inside an aggregation chamber with liquid nitrogen cooled walls. A flow of helium is used for collisional cooling of the C_{60} molecules. Estimated vibrational temperatures of $80°K$ are achieved.*
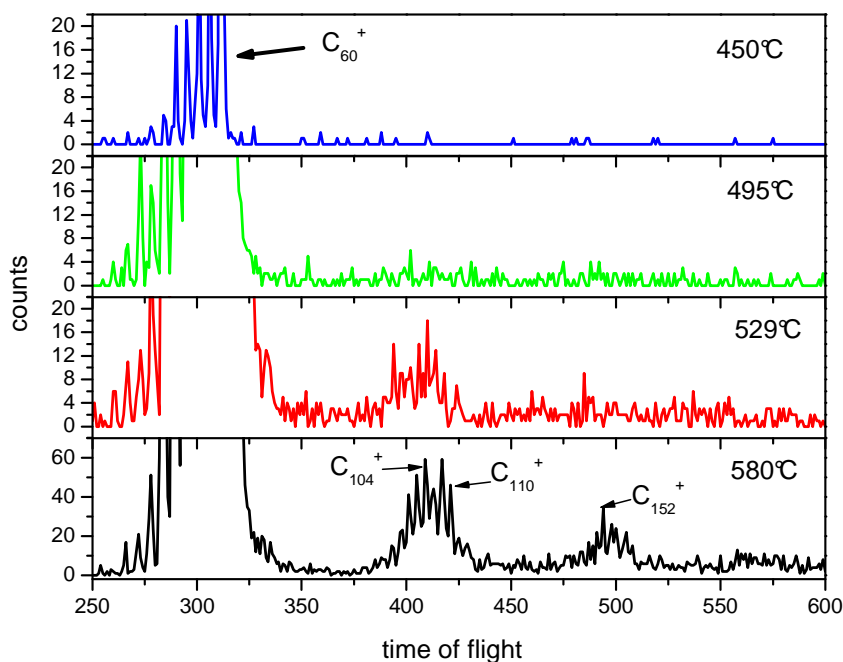

Figure 2.8: *Influence of the oven temperature in aggregation chamber on the mass spectra. As the temperature is increased, the density of C_{60} is increased and clusters of C_{60} are formed. The laser excitation was 800nm, 100 fs, and a fluence of 1 J/cm^2. The x-axis is in bins of 64 ns width, thus the resolution is reduced in comparison to other mass spectra in this work.*

then makes several round trips, gaining energy every time it passes the gain medium (crystal). After a selected number of round trips, the pulse is coupled out of the cavity, compressed, and sent to the experiment or further amplification stages. Outgoing energy per pulse for the present work was typically several hundred micro-Joules.

The second type of laser system is a multiple pass amplifier, which has the capability to reach shorter pulse durations by avoiding gain narrowing in the amplification gain medium. This is achieved by guiding the laser pulse to be amplified through a folded optical path which passes through the gain medium several times at different points.

Short pulse durations are important for determining the time dynamics of the excited molecule or ion. However, for photoelectron spectroscopy, it is desirable to have narrower energy bandwidths to distinguish between closely separated electronic states (or even vibrational states). For most of this work, a compromise was made between the two conditions.

Four different systems were used during this work and are briefly summarized in Table 2.1. The designated names are internal names for the laser systems, and are intended here to simplify description.

Table 2.1: *A table of the defining characteristics of the different laser systems used in this work. The working name, fundamental wavelength, bandwidth limited pulse duration, and energy bandwidth are given.*

LASER SYSTEM	Fundamental Wavelength	Bandwidth Limited Pulse Duration	Energy Bandwidth
Quantronix	800 nm	180 fs	10 meV
Clark	800 nm	100 fs	20 meV
Multicolor	800 nm	50 fs	40 meV
Multipass	800 nm	30 fs	75 meV

Quantronix Regenerative Amplification System

This system is a commercial, Ti:Sapphire oscillator and regenerative amplifier of the first generation, which delivers a maximum energy per pulse of approximately 400 μJ

in 180 fs.

The relatively narrow energy bandwidth of the Quantronix laser system allowed us to resolve the electronic structure observed in the photoelectron spectra. Consequently, the time resolution was not adequate for determination of intermediate, short-lived states. Furthermore, significant energy relaxation occurs on this time scale. Most of the single pulse Rydberg spectra were measured at this system.

Clark Regenerative Amplification System

This is a commercial (Clark MXR), Ti:Sapphire oscillator and regenerative amplifier system, delivering up to 600 μJ of energy per pulse in 100 fs.

This system provided the best compromise between time resolution and energy resolution for the experiments where both are needed. The energy resolution was sufficient to resolve several electronic peaks in the photoelectron spectrum, while also giving 100 fs time resolution.

This system was used for the measurement of time resolved photoelectron and photo-ion spectra, both one and two color, as well as position sensitive detection.

Through the implementation of an Optical Parametric Amplifier, wavelengths in the range between 600 and 700 nm were accessible. One experiment concerning the excitation of Rydberg states was performed with this device.

Multicolor Regenerative Amplification System

The Multicolor system is a commercial system, consisting of a Ti:Sapphire oscillator (Tsunami-Spectra Physics) and regenerative amplifier (Spitfire- Spectra Physics). The output pulse characteristics were up to 2 mJ of energy per pulse in 50 fs. This system was used for one color (800 nm) pump-probe measurements on the fragmentation dynamics of C_{60}.

Multipass Amplification System

The Multipass was used for experiments requiring very short pulses. It delivers pulse energies up to 500μJ with pulses as short as 30 fs, which provides a pulse significantly shorter than several vibrational modes and is also shorter than the electronic relaxation time. This system was used primarily for the results presented in the chapter on pulse shaping.

2.4   Laser Beam Characterization

2.4.1   Definition of Intensity and Fluence

Two very important characteristics of laser pulses are fluence and intensity. These two quantities determine the physical regime which occurs during laser - matter interaction, and must be considered for interpretation of results. Effects which occur under strong fields will be discussed in the next chapter.

The laser intensity of an ideal Gaussian laser pulse (TEM$_{00}$ electro-magnetic field) can be written as

$$I(r,t) = I_m exp(-(r/w)^2)exp(-(t/\tau)^2) \tag{2.6}$$

where I_m is the maximum laser intensity, $exp(-(r/w)^2)$ is the spatial distribution with w the beam waist at $1/e$, and $exp(-(t/\tau)^2)$ the temporal part with τ as the temporal width at $1/e$.

The integral of both the time and intensity profile over space and time gives the pulse energy as given in Eq. 2.7.

$$
\begin{aligned}
E_p &= I_m \int_{-\infty}^{\infty} exp(-(t/\tau)^2)dr \int_{0}^{\infty} exp(-(r/w)^2)dt \\
&= I_m\sqrt{\pi}\tau * \pi w^2 \tag{2.7}
\end{aligned}
$$

where E_p is the pulse energy, a directly measurable quantity. Rearranging the terms, the peak intensity, I_m is found to be

$$I_m = \frac{E_p}{\sqrt{\pi}\tau * \pi w^2} = 0.83\frac{E_p}{t_h d_h^2} \tag{2.8}$$

where $t_h = \tau/2\sqrt{\ln 2}$ and $d_h = w/2\sqrt{\ln 2}$ are the temporal and spatial FWHM, respectively. The peak intensity is dependent on three measurable paramters : pulse energy, pulse duration, and spatial width. Values of intensity are usually given in W/cm^2.

The two integrals can also be considered separately, giving two physically important parameters : the fluence and power. The fluence, or the amount of energy per

area, is the time integral of the intensity profile and is shown in Eq. 2.9

$$
\begin{aligned}
F(r) &= I_m exp(-(r/w)^2) \int_{-\infty}^{\infty} exp(-(t/\tau)^2)dt \\
&= I_m exp(-(r/w)^2)\tau\sqrt{\pi} \\
&= 0.883\frac{E_p}{d_h^2}exp(-(r/w)^2)
\end{aligned}
\tag{2.9}
$$

where $F(r)$ is the spatial dependent fluence. The peak fluence, $F(0)$ occurs when $r = 0$.

$$
F(0) = I_m\sqrt{\pi}\tau = \frac{E_p}{\pi w^2} = 0.883\frac{E_p}{d_h^2}
\tag{2.10}
$$

Fluence is usually given in units of J/cm^2.

On the other side, the integral of the intensity profile over space gives the pulse power (energy per time) and is shown in Eq. 2.11

$$
\begin{aligned}
P(t) &= I_m exp(-(t/\tau)^2) \int_{0}^{\infty} exp(-(r/w)^2)dr \\
&= I_m exp(-(t/\tau)^2)\pi w^2
\end{aligned}
\tag{2.11}
$$

where P(t) is the time dependent pulse power. At $t = 0$ the maximum power $P(0)$ is

$$
P(0) = I_m\pi w^2 = \frac{E_p}{\sqrt{\pi}\tau} = 0.940\frac{E_p}{t_h}
\tag{2.12}
$$

The pulse power is given in units of Watts [W].

In this work, only fluence and intensity (and primarily the later) are considered. The energy per pulse or average energy was determined by pyroelectric photo-detector (LTB) within a few percent. The pulse duration was measured with an auto- or cross-correlation technique or alternatively with the cross- Frequency Resolved Optical Gating (X-FROG) method. The experimentally difficult quantity to measure, particularly in situ, is the focal spot size.

2.4.2   Spatial Characterization of the Laser Beam

Since the focal spot size determines the interaction volume as well as the maximum intensity, it is very important to discuss the focal conditions. The laser beam was focussed with a $f = 30$ cm thin lens. Using Gaussian beam optics and assuming a

parallel input beam, w_0, one can calculate the beam waist, w_1, at the focal point of a lens by using the following relation:

$$w_1 = \frac{\lambda f}{\pi w_0} \tag{2.13}$$

where λ is the wavelength, and f is the focal length. This assumes, however, perfect focussing conditions. The values of w_0 and w_1 can be either the radius or diameter. It is thus better to measure the beam waist at the focus in situ.

The spot sizes were measured using the knife edge method, where a thin razor blade is moved across the focal spot and the intensity versus position is recorded. The derivative of this signal results in the beam profile. The profile for a TEM00 mode laser beam will have a Gaussian form, whose width is defined at 1/e intensity [DRu96].

The approximate beam waist spot sizes (FWHM) for the different laser systems are documented in Table 2.2 [1]. Also included are the peak intensities assuming a pulse energy of 100μJ and pulse duration characteristic of the laser system.

Table 2.2: *For a f = 30 cm lens, a characteristic spot size and pulse duration are used to calculate the maximum intensity at a laser pulse energy of 100 µJ. The values are calculated by Eq. 2.8.*

LASER SYSTEM	Diameter (d_h)	laser energy (E_p)	pulse duration (t_h)	Intensity @ 100 μJ (I_0)
Quantronix	100 μm	100 μJ	180 fs	$5*10^{12}$ W cm^{-2}
Clark	70 μm	100 μJ	100 fs	$2*10^{13}$ W cm^{-2}
Multicolor	70 μm	100 μJ	50 fs	$4*10^{13}$ W cm^{-2}
Multipass	50 μm	100 μJ	30 fs	$6*10^{13}$ W cm^{-2}

Due to uncertainties in measurement using the knife-edge method, determination of the intensity is also performed with the aid of Xenon photo-electron spectra, which have a well characterized structure at different intensities (see [SLH98, LTC98] or

[1]The spot size for the Multicolor system was not measured. The intensity was determined only with the photoelectron spectra of Xenon.

[Bor96]). An additional advantage of using Xenon is that it can be used to calibrate the energy scale of the electron spectrometer. The intensities used in this thesis remain consistent with those values in [Hof00]. Careful comparison of spectra (both Xe and C_{60}), allowed for an accurate determination of intensity.

The Rayleigh range, z_R is another common parameter used to characterize the laser beam focus and is the distance between the beam waist, w_0, and where the spot size has increased to $\sqrt{2}w_0$ along the axis of propagation. It is defined as

$$z_R = \frac{\pi w_0^2}{\lambda} \qquad (2.14)$$

where w_0 is the beam waist and λ is the wavelength. When the waist increases by a factor of $\sqrt{2}$, the intensity, I_m has decreased by a factor of 2. For the Clark system, where the diameter $(2w_0)$ is 50 μm and the wavelength is 800 nm, this corresponds to a Rayleigh range of 5 mm. This means that over a range of 1 cm along the laser beam propagation the peak intensity is within a factor of 2.

2.4.3   Temporal Characterization of the Laser Pulse

Characterization of the intensity and phase distribution in time and frequency of laser pulses is necessary for interpretation of data. This is particularly critical for shaped pulses, where the temporal pulse form can be complex. Three techniques have been used to characterize the laser pulses of the fundamental wavelength : auto-correlation, cross-correlation, and cross correlation frequency resolved optical gating (X-FROG). Shaped pulses are best characterized by either cross correlation or X-FROG measurements since they determine the temporal pulse form uniquely. The X-FROG measurement measures additionally a frequency spectrum at each time delay and can be used to reconstruct the temporal and spectral phase with an iterative, retrieval algorithm.

Auto-/Cross-correlation

Auto- and Cross-correlation are two basic (and similar) techniques used for determination of the time profile of a laser pulse. There are two types of auto-/cross-correlation, collinear and non-collinear. For this work, the non-collinear cross correlation was used most frequently. The mathematical formalism of these techniques are the same.

The general correlation function $G^n(\tau)$ of nth order for two functions S_1 and S_2 is

$$G^n[S_1(t), S_2(t)](\tau) = \int_{-\infty}^{\infty} \left|(S_1(t) + S_2(t - \tau))^n\right|^2 dt \qquad (2.15)$$

When $S_1(t){=}S_2(t)$, the correlation is considered to be the autocorrelation. The auto- or cross-correlation of laser pulses is often measured with a non-linear crystal, therefore the correlation function of second order is particularly important to consider.

$$G^2(\tau) = \int_{-\infty}^{\infty} \left|((\mathcal{E}_1(t) + \mathcal{E}_2(t - \tau))^2\right|^2 \qquad (2.16)$$

where $\mathcal{E}_i$ represents the electric field of the laser. For a cross-correlation apparatus in non-collinear orientation, the second order intensity cross correlation is given by[DRu96]

$$A(\tau) = \int_{-\infty}^{\infty} I_1(t) I_2(t - \tau) dt \qquad (2.17)$$

This is the so called background free correlation. For auto correlation, the pulses are identical and $\mathrm{I_1}$ and $\mathrm{I_2}$ are equivalent.

Cross correlation is experimentally carried out in the following manner: two replica pulses are generated using a beamsplitter, a reference pulse $E_r(t)$, and a test pulse $E_{test}(t)$. The two pulses travel different pathways, yet similar optical lengths. The reference pulse remains unaltered, typically of bandwidth limited pulse duration. It is advantageous to have a short reference pulse, since the measured pulse is a convolution of the the reference pulse and the test pulse. The second pulse is temporally altered in its pathway, for instance by a pulse shaper, as shown in Fig. 2.9. The two pulses are spatially and temporally overlapped on a nonlinear SHG crystal, a Type II Barium Borate (BBO) crystal of 50μm thickness. The reference pulse is scanned in time. The resulting intensity is proportional to the product of the input pulse intensities and is described mathematically by Eq. 2.17.

X-FROG

The frequency resolved optical gating (FROG) method is used to measure pulses in the coupled time-frequency domain [KTr93]. This is accomplished by measuring the frequency spectrum for each time delay to build a spectrogram, also known as a "FROG trace". There are four main techniques of performing FROG, Second Harmonic Generation (SHG), Third Harmonic Generation (THG), Polarization Gating (PG), and Self Diffraction (SD). In this work, SHG cross correlation FROG (SHG-XFROG) has
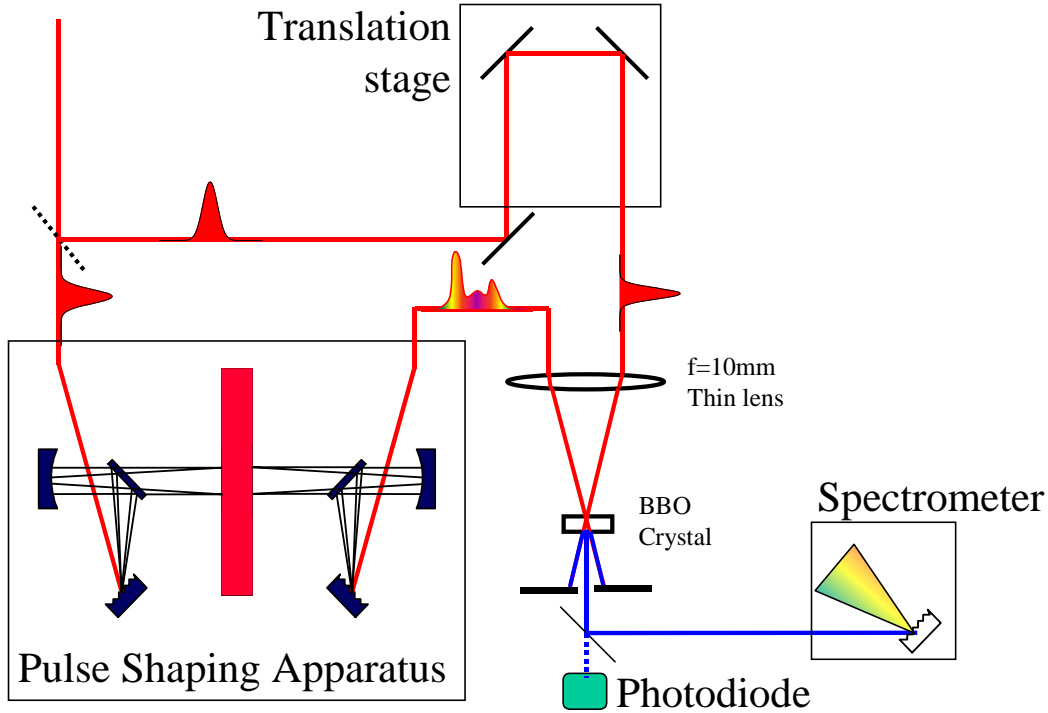
Figure 2.9: *Set up for temporal characterization of shaped (and unshaped) laser pulses. The cross correlations were recorded the second harmonic signal with the photodiode, while the X-FROG pictures were measured with the spectrometer.*

been used. In this technique, an unmodulated pulse functions as the gate and is, in principle, different from the modulated test pulse. Similar to the difference between auto- and cross-correlation, the SHG-XFROG spectra will be asymmetric, whereas the SHG-FROG is temporally symmetric.

The apparatus setup is the same as shown in 2.9. However, for each time delay, the spectral intensity is measured with a spectrometer (AvaSpec 2048, spectral range 333nm-481nm, with a resolution of $\Delta\lambda = 0.1$ nm) rather than recording the integrated intensity. This provides additional information about the spectral components, which can be used to fully reconstruct the electric field. The resulting spectrogram can be mathematically described as

$$S(\omega, \tau) \equiv \left| \int_{-\infty}^{\infty} \mathcal{E}_{cc}(t)g(t - \tau)e^{-i\omega t}dt \right|^2 \tag{2.18}$$

where $g(t-\tau)$ is the variable delay gate function. In the present case of laser radiation, $g(t - \tau) = \mathcal{E}_t(t - \tau)$.

After the frequency vs. time contour plot is recorded, an iterative phase-retrieval algorithm can be used to calculate the amplitude and phase of the test pulse to give quantitative values of these properties. The algorithm operates on the technique of generalized projections. There are two constraints which must be satisfied[LGK98], the mathematical form must have the form of the nonlinear process generating the pulse, i.e., for SHG the optical constraint can be written as

$$\mathcal{E}_{cc}(t,\tau) = \mathcal{E}(t)\mathcal{E}(t-\tau) \tag{2.19}$$

and the squared magnitude of the fourier transformation must conform to the measured data

$$I_{XFROG}(\omega,\tau) \propto \left| \int_{-\infty}^{\infty} \mathcal{E}_{cc}(t,\tau)e^{-i\omega t}dt \right|^2. \tag{2.20}$$

which says that the measured intensity is proportional to the electric field of the cross correlation.

The algorithm begins with a guess of the electric field $\mathcal{E}_{cc}(t,\tau)$. During one iteration, the algorithm looks for the closest point on the adjacent constraint set, which is implemented by Fourier transformation. The unique solution is located at the intersection of these two subsets. The deviation is systematically reduced until the algorithm converges. The algorithm operates as shown in the block diagram of Fig. 2.10.
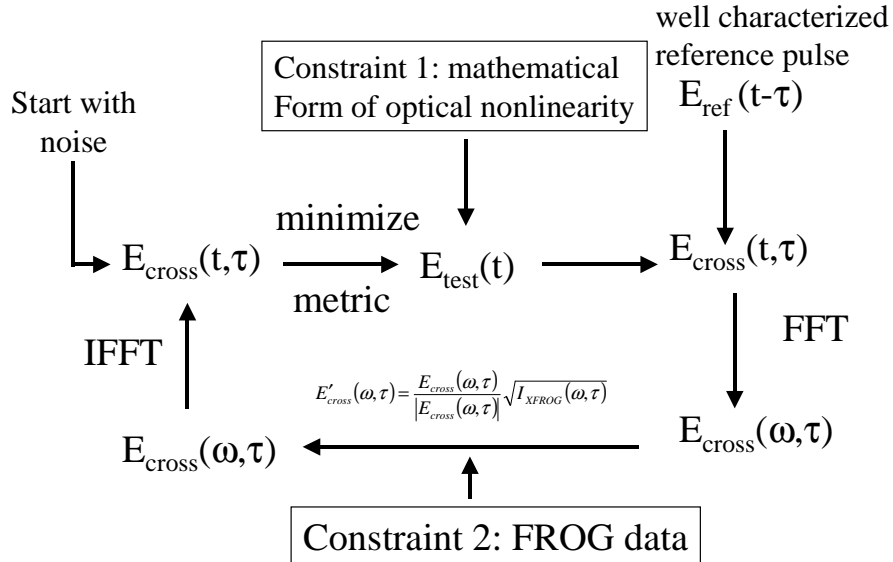

Figure 2.10: *General XFROG algorithm for calculating the amplitude and phase of the test pulse (from [LGK98])*

where IFFT is the inverse fast Fourier transform with respect to frequency, and FFT is the fast Fourier transform with respect to time. The phase retrieval algorithm used in this work is from Femtosoft.

The ordinate of the FROG trace is the frequency axis and the abscissa is the time axis. A qualitative analysis can be quickly made simply by observation of the spectrogram. Second and third order dispersion and multiple pulses can all be easily identified. Chirp, which is defined as the change in frequency versus time, can be qualitatively recognized in X-FROG spectra as diagonal lines either increasing with time (up-chirp or positive chirp) or decreasing with time (down-chirp or negative chirp) as is shown in Fig. 2.11.

The FROG spectrum of an amplified pulse at the Multipass laser system is presented in Fig. 2.12(left). The measured temporal width is found to be 30 fs, however, the spectral width indicates that a shorter pulse is possible. This is further indicated by the calculated spectral phase, plotted in Fig. 2.12(right), where a quadratically curved spectral phase which indicates that predominantly second order dispersion is present in the measurement. The spectral phase is compared to a pure quadratic curve. This dispersion may arise from extra glass in the optical path.

2.5   Time of Flight Spectroscopy

Time-of-flight (TOF) spectroscopy is a basic and common technique used for gas phase studies. It is the measurement of the amount of time needed for a charged particle to reach a detector after an ionization event. The time needed to reach the detector is proportional to the momentum of the charged particle. In ion TOF spectroscopy, this implies the observation of different times for different masses. In electron TOF spectroscopy, the time of flight is related to the kinetic energy. Despite its simplicity, the information which can be drawn is very sophisticated.

Four different time-of-flight (TOF) configurations were used during this work.

1. Linear ion TOF (detector: MCP2 in Fig. 2.13)

2. Reflectron ion TOF (detector: MCP3 in Fig. 2.13)

3. Linear electron TOF (detector: MCP1 in Fig. 2.13)

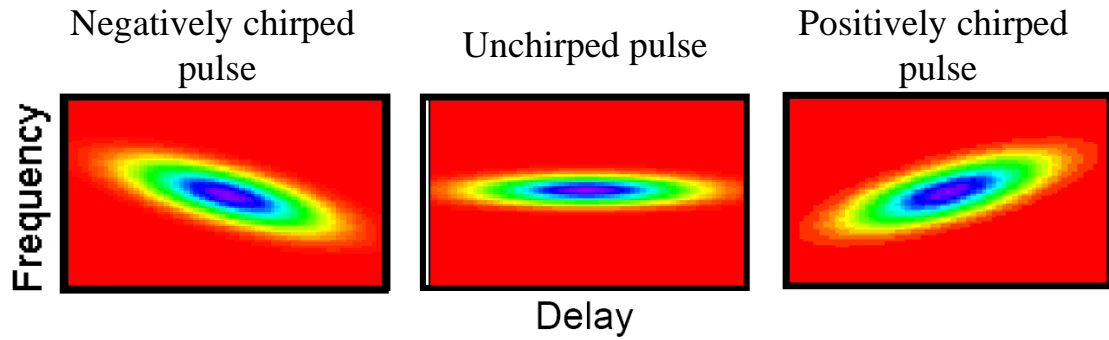4. Linear ion TOF with position sensitive detector (see Fig. 2.22)

Figure 2.11: *Examples of negatively chirped, unchirped, and positively chirped XFROG spectrograms (From R.Trebino).*
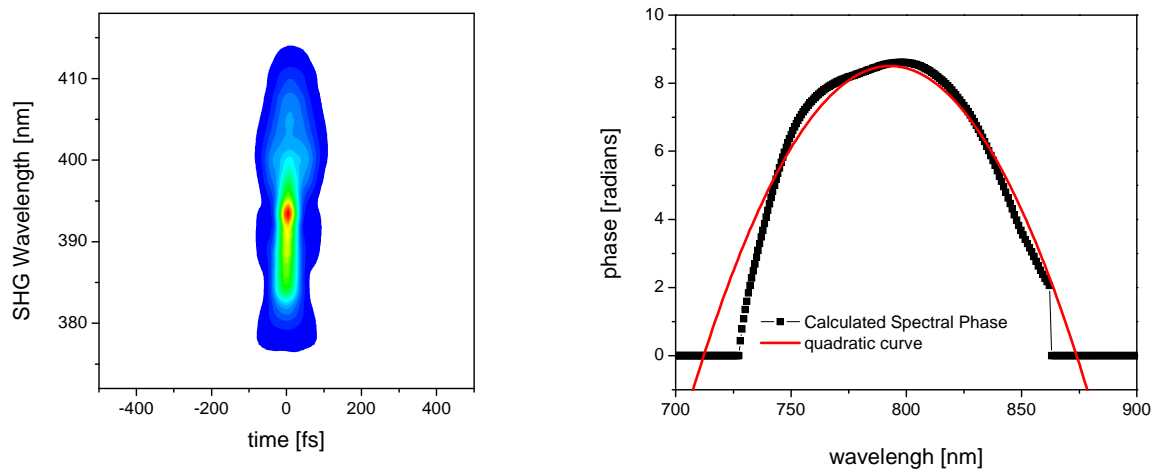

Figure 2.12: *FROG spectrogram of unmodulated pulse form at the Multipass laser system. On the right hand side of the figure, the calculated spectral phase is shown, the predominantly quadratic curve indicates a second order dispersion.*

The first three detectors are shown in Fig. 2.13. The fourth was built in the context of this thesis in a separate apparatus, and attached where the electron spectrometer is located in Fig. 2.13 (see Section 2.6 for more details). In each case, including the linear TOF with position sensitive detector, the excitation region was located at the center between M_2 and M_3, i.e., 1 cm $\pm$ 1 mm from M2 and M3. The position of the laser beam was checked prior to evacuation by placing a paper between the two meshes. During the experiment, the narrow entrance and exit windows (for the laser) of the vacuum chamber ensured a constant alignment. A schematic of the TOF apparatus used in this work is shown in Fig. 2.13.
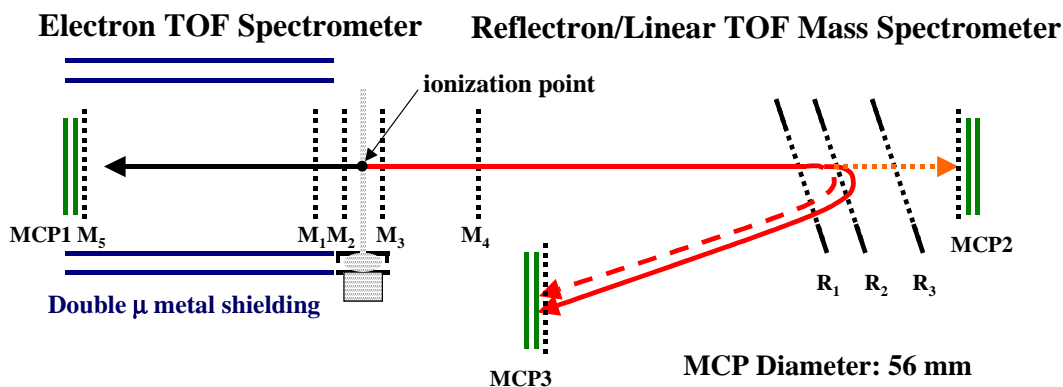

Figure 2.13: *Detailed schematic of apparatus showing the electron and ion spectrometer. The meshes are shown as dashed lines, and the MCP pairs are denoted with a double bar. The excitation point is in the middle between M_2 and M_3. The size of the MCPs are the limiting lateral dimension. The diameter of the MCPs is 56 mm.*

The apparatus allowed for rapid changing between ion and electron TOF detection, i.e., keeping constant laser, vacuum, and molecular beam conditions, but was inadequate for coincidence measurements because the pressure in the interaction region was too high (10^{-7} Torr) to reduce false coincidences from background gas for the laser intensity needed to ionize C_{60}.

Deflection Plates

One alteration to the time of flight apparatus was needed for the cold molecular beam source. Since the velocity distribution is no longer thermal, as is the case for the "hot source", but rather supersonic, with an estimated speed of 1000 m/s (speed of helium), electric deflection of the ions were necessary for additional guiding of ions onto the

MCP detector. Both vertical and horizontal plates of length 35 mm were inserted in the field free region just after the second voltage region of the Wiley-McLaren set-up, as is shown in Fig. 2.14. Adjustment of the voltage placed on the plates allowed for the guidance of ions onto the MCP. The acceleration voltages were not changed. The plates were grounded for (further) experiments with the "hot source".
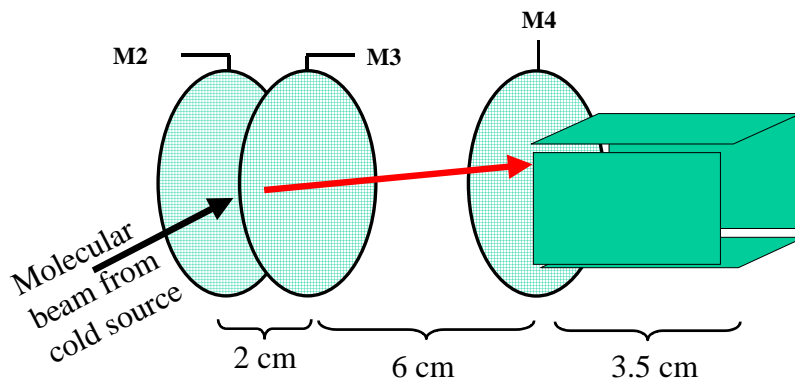

Figure 2.14: *The deflection plates added to accommodate for the fast translation motion of molecules from the "cold source".*

2.5.1   Ion Time of Flight Spectroscopy

For detection of ions, both a linear and a reflectron time-of-flight spectrometer built in a Wiley-McLaren configuration [WMc55] were used. The Wiley-McLaren configuration has two extraction regions of different acceleration voltages. This has the advantage over single plate acceleration regions because it provides both a temporal and spatial focussing of the ions.

The potentials applied to the meshes and the spacing of the meshes for use of the reflectron or linear time of flight are listed in Table 2.3.

The length of the linear TOF from interaction point to MCP is 190cm. Since there is no instrumental acceleration on the axis perpendicular to the TOF axis, ions with "large" velocities in this direction will not be detected. The maximum detected velocity is dependent on the time of flight, i.e., mass and acceleration voltage, and the active MCP radius. The maximum perpendicular velocity for C_{60} is approximately 350 m/s for a flight time of 71 μs.

An exemplary mass spectrum measured with a linear TOF is shown in Fig. 2.15

Table 2.3: *The table on the left show the typical voltages used during the present work and the table on the right shows the distances between the different meshes. GND denotes ground or earth. The size of the MCPs are the limiting lateral dimension. The diameter of the MCPs is 56 mm.*

MESH	Linear TOF	Reflectron TOF
M_1	GND	GND
M_2	+2470 V	+2470 V
M_3	+2076 V	+2076 V
M_4	GND	GND
R_1	—	GND
R_2	—	+1676 V
R_3	—	+2800 V

MESH pair	distance
M_1-M_2	0.5 cm
M_2-M_3	2 cm
M_3-M_4	6 cm
M_4-R_1	153 cm
R_1-R_2	2.6 cm
R_2-R_3	23.4 cm
R_1-MCP3	108.6 cm
M_4-MCP2	190 cm

after femtosecond pump-probe excitation. These two plots illustrate the complexity of the C_{60} fragmentation pattern under interaction with femtosecond laser pulses. Prominent single and double charged heavy fragments are present and additionally singly charged lighter fragments. The right hand side of Fig. 2.15, shows an expanded view of the small fragments between C^+ and C_6^+. This spectrum will be further discussed in Chapter 5.

The resolution of a Wiley-McLaren TOF apparatus is determined by several parameters, such as the drift length, spatial distribution in the acceleration region, velocity distribution parallel to the TOF axis[WMc55], and time resolution of the detector and time to digital converter (TDC). The width of the focal volume along the TOF axis does not affect the resolution of our Wiley-McLaren spectrometer, as the spatial distribution results in a time difference less than the bin size of the time to digital converter. The experimental peak widths primarily result from the velocity distribution of the molecular beam and kinetic energy from fragmentation. The C_{60} peak width is ideally zero, assuming only ionization. The so called "apparatus width" for C_{60} is slightly greater than the time resolution of 16 ns of the TDC at full-width-half-maximum (FWHM). The apparatus width is linearly dependent on the mass, which means the apparatus width of C^+ and C_2^+ are negligible with respect to the
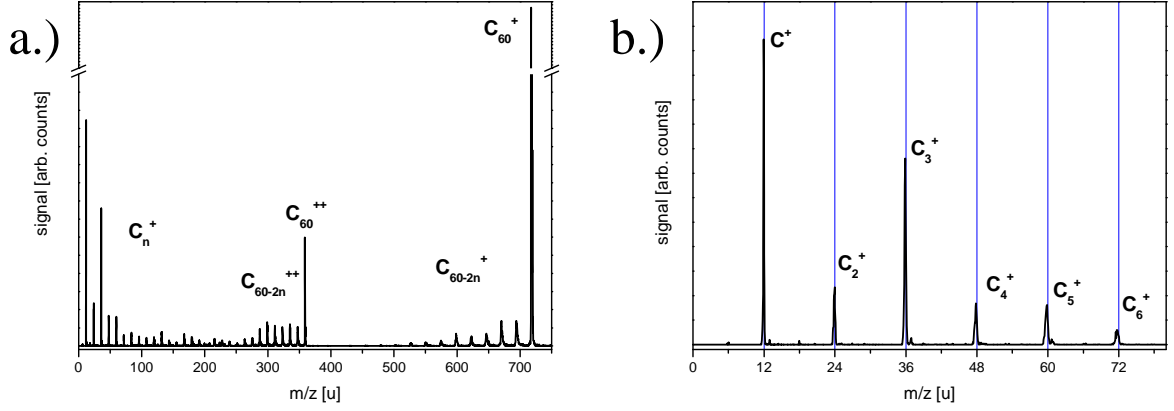
Figure 2.15: *Example of the C_{60} mass spectrum observed with a linear TOF after femtosecond pump-probe excitation. Graph a.) shows the complete mass spectrum. Graph b.) displays an expanded view of the small fragments. Pump pulse: 400 nm, 120 fs, $4*10^{12}$ W/cm^2 Probe pulse: 800 nm, 120 fs, $5*10^{12}$ W/cm^2.*

width of the bins time resolution.

The width of the mass peaks in a time of flight spectrum is also dependent on the initial kinetic energy of the charged particle. The width can be understood through the difference in time-of-flight of two particles with equivalent kinetic energies created at the excitation point and fly in opposite directions (see Fig. 2.16). The particle which moves away from the collector (particle a) will return to the excitation point with the same energy, and its subsequent motion will be identical to the ion which initially moves toward the detector (particle b). The time difference between particle a and b to reach the detector is twice the time necessary to stop an ion with initial velocity away from the detector. This time is often called the "turn-around time" and determines the width of the mass peak.

To calculate the "stopping time" ($= \frac{1}{2}*$"turn-around time), one needs only to consider conservation of energy. The resulting kinetic equation must be solved for the time difference, Δt,

$$v_f = v_i + a\Delta t \tag{2.21}$$

where v_f and $v_i = \sqrt{2mE_i}$, with initial kinetic energy E_i and mass m, are the final and initial velocities, respectively, and the acceleration $a = \frac{ze_0\mathcal{E}_s}{m}$ with electric field $\mathcal{E}_s$ and charge ze_0. The final velocity (at the turning point) is 0.
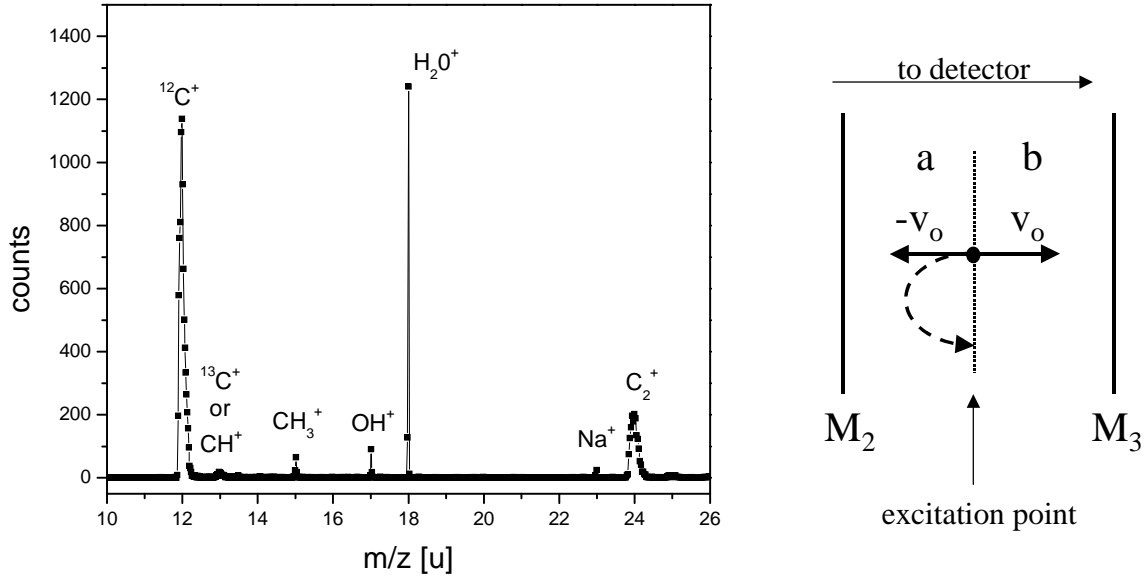
Figure 2.16: *Example of the C_{60} mass spectrum observed with a linear TOF after femtosecond pump-probe excitation. The left hand side shows a small portion of a mass spectrum, highlighting the difference of mass peak widths between carbon fragments and background gases. This mass spectrum was measured in the ReTOF. On the right hand side displays a small schematic demonstrating the time difference between two particles with equal but opposite velocities. M_2 and M_3 refer to the meshes in Fig. 2.13. Pump pulse: 800 nm, 50 fs, $5*10^{13}$ W/cm^2 Probe pulse: 800 nm, 50 fs, $2.5*10^{13}$ W/cm^2.*

The peak width, ΔT, is given by Eq.2.22 [WMc55].

$$\Delta T = 2 * \Delta t = \frac{2\sqrt{2mE_i}}{ze_0\mathcal{E}_s} \tag{2.22}$$

This equation is valid for linear time-of-flight apparatuses. For a reflection time-of-flight apparatus, the reflection of the ions must be further considered, but under proper settings, the width can be clearly seen as is observed on the left hand side of Fig 2.16, the width of the carbon mass peaks are significantly wider than the width of background gases such as H_2O^+.

The width of mass peaks measured with a *linear* time-of-flight were analyzed by fitting the mass peaks with a Gaussian. The FWHM of the mass peaks was found and using Eq. 2.22 the kinetic energy was calculated. An example is shown in Fig. 2.17 for C^+. The fit shows that a Gaussian is not the perfect fit, however, this allowed for rapid quantitative calculation of thousands of spectra and different masses.

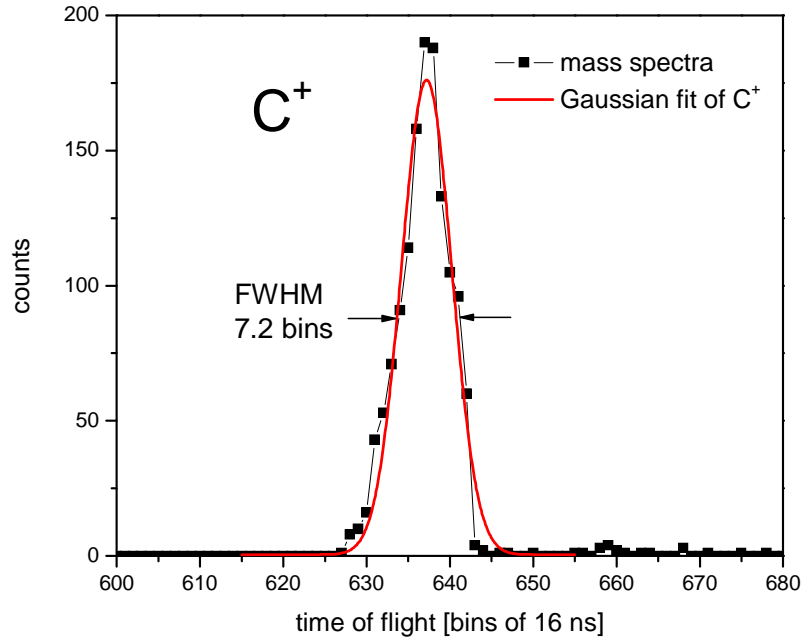The reflectron time of flight (ReTOF), historically, was developed to increase mass

Figure 2.17: *Gaussian fit of C^+ mass peak measured in a linear time-of-flight. The excitation source in this case was with two color pump-probe. Pump pulse: 400 nm, 120 fs, $4*10^{12}$ W/cm^2 Probe pulse: 800 nm, 120 fs, $5*10^{12}$ W/cm^2 with a time delay of 200 fs.*

resolution, while also conserving limited laboratory space. The reflecting voltages can be applied to compensate the energy distribution, which in addition to the enhanced length, increases the mass resolution. In the present apparatus, the flight of the ions begins similarly as in a linear TOF, however at the end of the vacuum chamber, rather than strike a MCP, the ions are reflected at an angle of 2° with respect to the time of flight axis. The length of the time of flight is increased by about 2 m. The resolution of the ReTOF in the present configuration is $m/\Delta m \approx 2900$ (at FWHM)[Hof00]. In comparison, the linear TOF has a $m/\Delta m \approx 1800$.

A second advantage is that fragmentation events that occur in the first field free drift tube can be detected. This consists of fragmentation occurring between ~ 2 μs and the time needed to reach the turning point of the reflectron (~ 60 μs for C_{60}). This fragmentation is called metastable fragmentation.

Fig. 2.18 shows an example of a spectrum measured with the reflectron TOF after one-color pump-probe excitation. The graph on the left shows the complete mass spectrum, while on the right an expanded view of the double charged fullerene fragments is shown. The metastable fragments are denoted with a (*). One disad-

vantage of the ReTOF apparatus is that the shape of the peak does not directly give information about the kinetic energy.
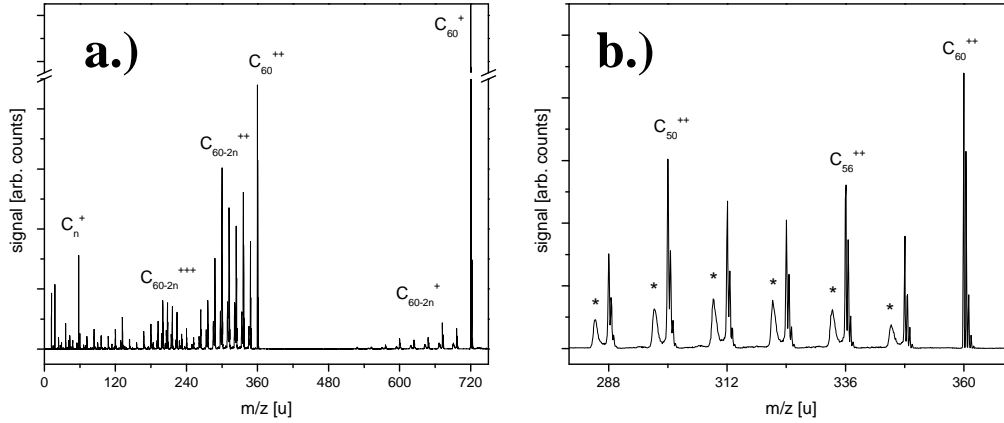

Figure 2.18: *Example of the C_{60} mass spectrum observed with a reflectron TOF after femtosecond pump-probe excitation. Graph a.) shows the complete mass spectrum. Graph b.) displays an expanded view of the double charged fullerene fragments. The (*) denotes the metastable fragmentation. Pump pulse: 800 nm, 50 fs, $5*10^{13}$ W/cm^2 Probe pulse: 800 nm, 50 fs, $2.5*10^{13}$ W/cm^2.*

Collection Efficiency

Since the area of the MCPs is small with a diameter of 56 mm and the length of the time-of-flight is long, the acceptance angle for fragments is quite small. The spatial distribution of the ionic "cloud" can be observed by varying the deflection voltage applied to the deflection plates in Fig. 2.14, which alters the number of ions incident onto the MCP detector. Fig. 2.19 shows the influence of deflection voltage on the ion yield for C_{60}^+, C_{60}^{++}, $\sum C_{60-2n}^+$, $\sum C_{60-2n}^{++}$, and C_1^+. The excitation was with two color pump-probe at zero time delay where the 800 nm pulse had an intensity of $5*10^{12}$ W/cm^2 and the 400 nm pulse had $4*10^{11}$ W/cm^2. The deflection was scanned in the horizontal axis perpendicular to the molecular beam axis and to the time of flight axis. The spatial distribution of C_{60}^+ and C_{60}^{++} is the most narrow since they do not fragment, followed by the large fullerene fragments, and finally C^+ which has significant KE from the fragmentation event due to its light mass.

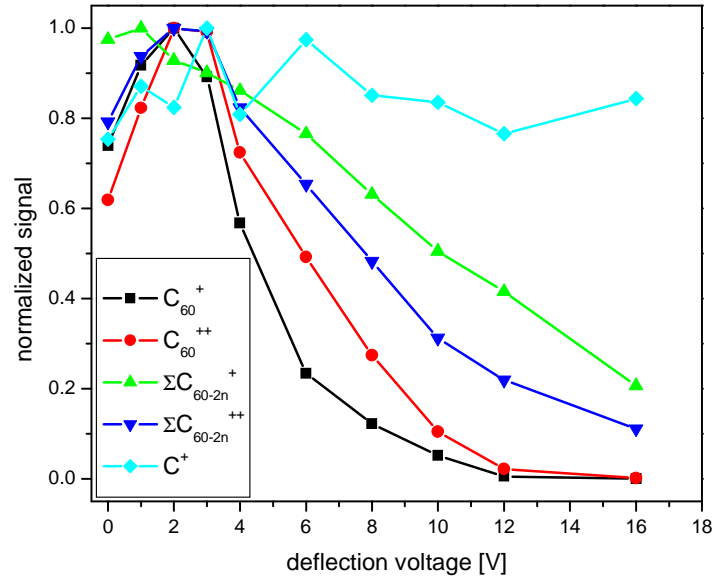The collection probability of a particle as dependent on the kinetic energy is given

Figure 2.19: *Influence of ion yield in the linear time of flight versus deflection voltage applied to the deflection plates in Fig. 2.14. The ions were created with pump-probe excitation. The laser conditions were 800 nm at $5*10^{12}$ W/cm^2 and 400 nm with $4*10^{11}$ W/cm^2.*

by (see Appendix C for details):

$$W = \left[1 - \sqrt{1 - \left(\frac{r}{d_z \sqrt{\frac{E_k}{Z*U}}} \right)^2} \right] \tag{2.23}$$

where E_k is the kinetic energy, d_z is the length of the time-of-flight, Z is the charge, and U is the acceleration potential. This calculation has been made for the linear time-of-flight as well as the position sensitive detector.

2.5.2 Electron Time of Flight Spectroscopy

The electron TOF is measured similarly to the ions. The potentials and distances of meshes are listed in Table 2.4. After excitation, the molecule will emit an electron with a certain kinetic energy and direction. To measure electron time of flight spectra no extraction field was applied. Since there is a fixed time resolution of our TDC (500ps), the use of extraction fields reduces the energy resolution. Since no extraction field
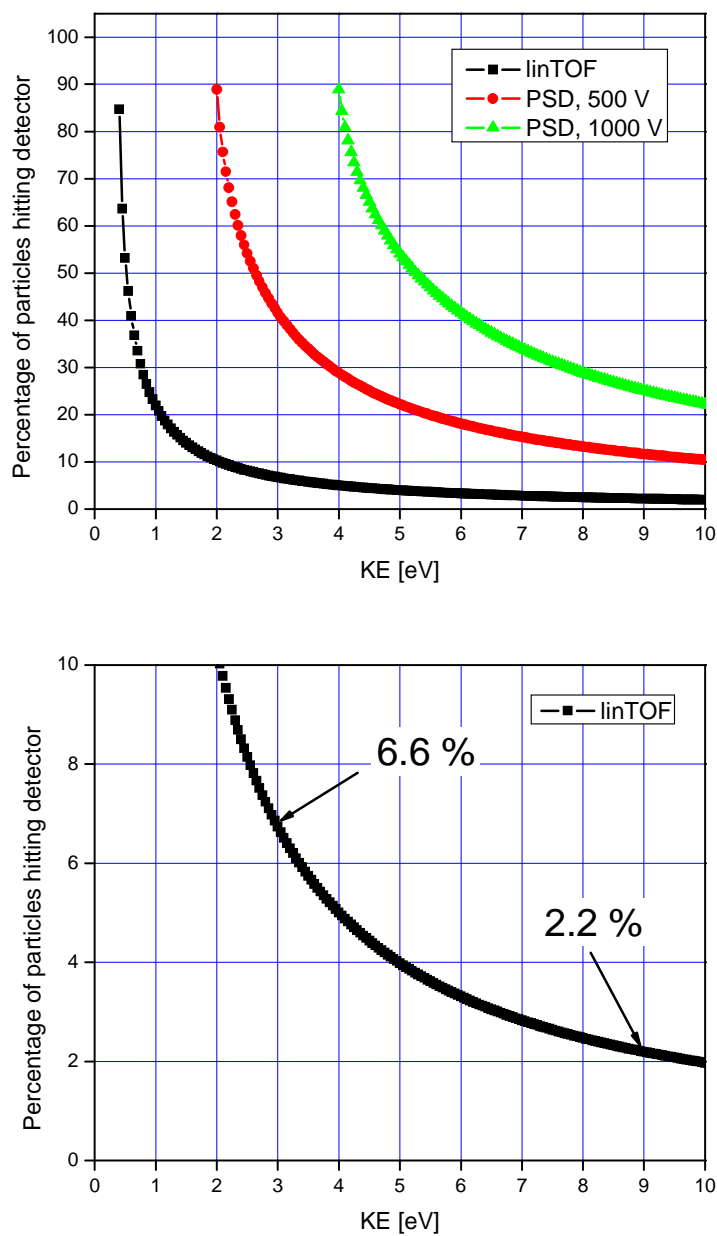
Figure 2.20: *Particle collection probability for three different ion TOF configurations used in this work. The bottom graph shows a close up of the linear time of flight, indicating the percent of particles collected at 3 eV and 9 eV. These values correspond to the measured kinetic energy of C^+ fragments in a pump-probe measurement.*

Table 2.4: *The table on the left show the typical voltages used during the present work and the table on the right shows the distances between the different meshes for the electron spectrometer. GND denotes ground or earth. The diameter of the MCPs is 56 mm. See Fig. 2.13 for the labelling of meshes.*

MESH	Electron TOF
M_1	GND
M_2	GND
M_3	GND
M_4	GND
M_5	GND

MESH pair	distance
M_1-M_2	1 cm
M_1-M_5	42 cm
M_5-MCP1	1 cm
M_2-M_3	2 cm

is used, only a small solid angle is measured which is determined by the size of the active area of the detector and only a small number of electrons emitted are actually detected. The distance to the detector from the interaction point is 45 cm and the active area of the MCP is approximately $\pi*(25 \text{ mm})^2$. The solid angle is defined as A/R^2, thus the solid angle for the electron detector is 9.7 msr, which is equivalent to a polar acceptance angle of $\sim 3.2°$. In comparison, a magnetic bottle TOF electron detector collects up to 2π sr of the complete sphere of $4*\pi$ sr.

The electrons must be shielded from magnetic fields, e.g. from the earth or induced by current, or the Lorentz force will dictate their motion and drive them in a helical path, which might miss the detector. A double mu-metal shield has been installed for the entire length of the drift tube (45 cm), and reduces the axial magnetic field by around four orders of magnitude.

The spectra were recorded in time with a resolution of $dt = 500$ ps. The distribution can be written as $f(t)dt$. The conversion to energy proceeds over the following relations:

$$E(t) = \frac{1}{2}m_e \left(\frac{L}{t}\right)^2 \tag{2.24}$$

and

$$f(E)dE = \frac{m_e L^2}{t^3} f(t)dt \tag{2.25}$$

where m_e is the mass of the electron and L is the length of the time of flight. The second equation accounts for the Jacobian for changing coordinates.

Due to the uncertainty in the absolute time zero, the energy scale must be calibrated with several lines of a known species. Xenon was used to calibrate the energy scale for both 800 nm and 400 nm. The time resolution is determined by the analog to digital card and is 0.5 ns. This means that the energy resolution of the electron spectrometer ranges from 5 meV at $E_{el} = 1$ eV to 400 meV at $E_{el} = 20$ eV.

2.5.3   Charged Particle Detection and Data Acquisition

The detectors used for both traditional ion and electron TOF experiments were multichannel plates(MCPs), which are leaded-glass discs that contain numerous pores. The inside of each pore is coated with lead oxide (PbO) and will readily release an electron or secondary electron when struck by an incident particle (or photon). Two MCPs were v-stacked in the chevron configuration, which means the channels were oriented oppositely for example at +15 and -15 degrees with respect to the MCP plane, allowing for optimal gain. This configuration typically results in a total gain of 10^8. The signal was further enhanced by a Novalek pre-amplifier (ions only) and discriminated before going to the time-to-digital converter TDC.

The acquisition of the electrical signal was made by a multi-scaler card with up to 2 GHz resolution (FastCom, Model 7886). For ions, 32 bins were grouped together resulting in 16 ns time resolution. Electrons were measured with the maximum time resolution of 0.5 ns.

The acquisition was handled by the W7886 program that was provided by the FastCom company. This basic program was inserted into self developed LabView routines to automate the measurements, such as pump-probe measurements or optimization algorithms.

2.6   Position Sensitive Detection

Position sensitive detection of charged particles increases the amount of information that can be extracted during a single measurement and has become a popular technique in atomic and molecular physics. The detectors are placed in TOF apparatuses, and for each event (charged particle or photon), the time and position (x-coordinate

and y-coordinate) are recorded. There are three common ways to detect the position of charged particles: segmented anodes, phosphor screens, and delay lines.

This section will describe the construction and properties of a ultrahigh vacuum apparatus in which a position sensitive, charged particle detector (Roentdek DLD-80) has been implemented. The design was made to accomodate electrons, which because of their light mass, require shielding from magnetic fields, however, the first results were performed with ions.

2.6.1   Construction of Vacuum Chamber for PSD

The vacuum apparatus was designed to be attached to the current vacuum apparatus (placed in the position of the electron spectrometer) as well as to conform to the future ultrahigh vacuum apparatus to be constructed. Therefore, the connection of flanges and chambers use CF flanges.

The cylinder was built from V4A steel, which has very low magnetic susceptibility. The inner diameter is 150 mm and its length is 400 mm. Four connections are present. One CF-35 flange for a pressure gauge, one CF-100 flange for a turbo molecular pump(Pfeiffer Vacuum TMU 261 - 210 L/s), and two CF-150 flanges, one for the detector and one for the connection to the interaction region chamber. Fig. 2.21 displays a cartoon of the vacuum apparatus in which the position sensitive detector was placed.

The distance from the interaction region to the front of the MCP stack is 45 cm (see Fig. 2.13). The laser-matter interaction occurs in the center of a 2 cm acceleration region, defined by meshes M2 and M3. The nomenclature from Fig. 2.13 has been preserved. A third mesh, M6, is placed 1 cm in front of the MCP to keep the electric field out of the field free drift tube. Both M2 and M6 are set to ground, the field free path is 43 cm. Wiley-McLaren conditions were not achieved for the acceleration of charged particles for position sensitive detection. For detection of ions, M3 was set to a fixed positive voltage. For detection of electrons (not done in this work), M3 would be set to ground or a small negative potential. Refer to Table 2.5 for a list of applied voltages and mesh separations.

Attenuation of the magnetic field is essential for photoelectron spectroscopy, as the Lorentz force can significantly alter the lateral position of a charged particle. Great detail has been made to design proper shielding for photoelectron spectroscopy with the position sensitive detector (see Appendix D). Essentially two concentric
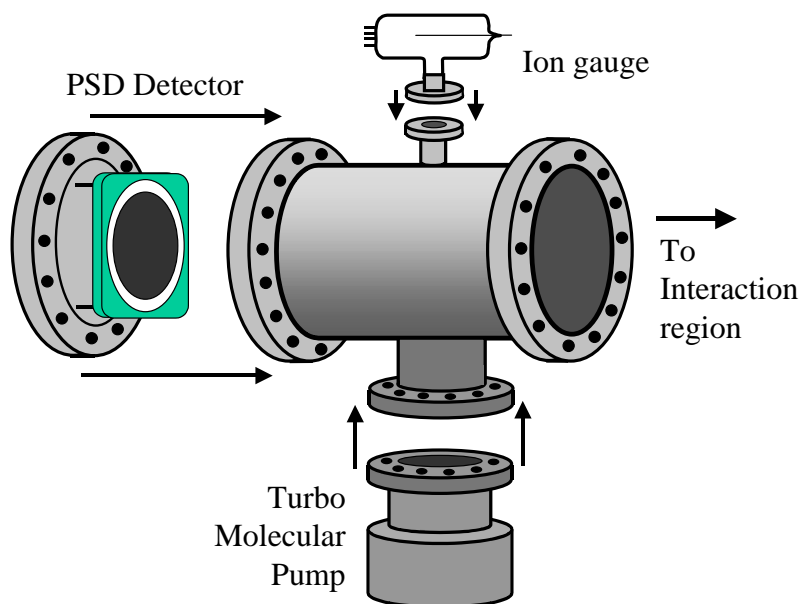
Figure 2.21: *Schematic of vacuum apparatus for position sensitive detector. The detector is directly attached to the flange, which is connected to the vacuum chamber with a CF-150 ring.*
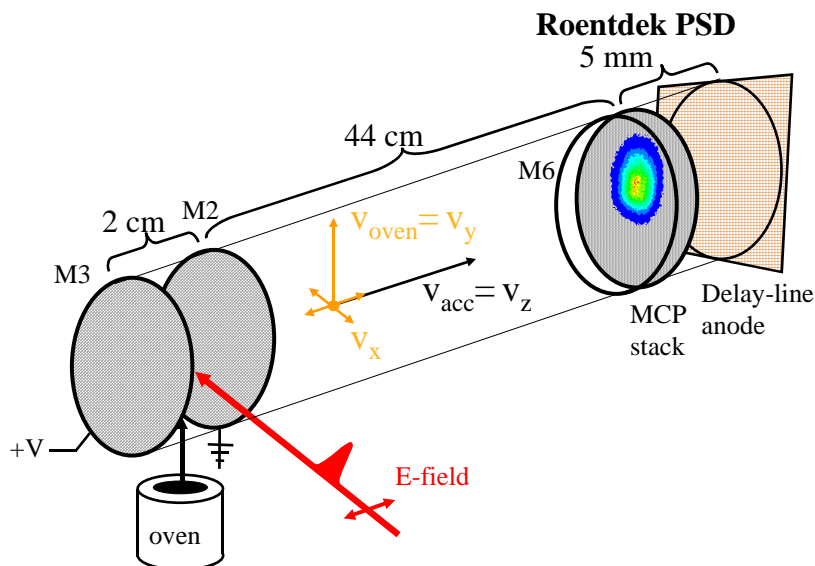

Figure 2.22: *Schematic of the time of flight geometry for position sensitive detector. The typical voltages applied to the meshes are listed in Table 2.5.*

Table 2.5: *The table on the left show the typical voltages used during the present work and the table on the right shows the distances between the different meshes for the position sensitive detection spectrometer. GND denotes ground or earth. The diameter of the MCPs is 80 mm. See Fig. 2.22 for labeling of meshes. M6 is a new mesh which functions as M5 in the electron spectrometer.*

MESH	PSD TOF
M_2	GND
M_3	500 V or 1000 V
M_4	GND
M_6	GND

MESH pair	distance
M_2-M_3	2 cm
M_2-M_6	43 cm
M_6-MCP	1 cm

circles are used to reduce the magnetic field several orders of magnitude and reduce the lateral displacement to a distance smaller than the pixel dimensions (0.25 mm) of the position sensitive detector.

2.6.2   Position Sensitive Detector, Electronics, and Software

A Roentdek DLD-80 3-D detector [JMU98, ADJ99] was implemented into the vacuum chamber described in the previous subsection. The device measures the TOF, as well as the position x and y, to characterize the charged particle (or photon) resulting from, for example, laser interaction.

Fig. 2.23 displays the construction of the detector. From top to bottom, there is a mesh, MCP pair, delay lines, and isolated (from detector and from flange) stainless steel holder. The mesh is set to ground and used to create a uniform field across the detector. Without the mesh, the image is strongly distorted.

Next there are two MCPs (Galileo, 80mm diameter), stacked in the chevron configuration. The determination of the TOF is done in a similar fashion as discussed in a previous section. The incident particle creates a cascade of electrons in the MCP. The resulting electric signal is then recorded using a time-to-digital converter (TDC)(LeCroy3377), operated in the common start mode. In this mode, the clock is started by the trigger and the time until an ion arrives is measured. The start trigger came from a photodiode signal created by a laser pulse. The photodiode was located about 3 meters from the interaction region. The true time zero is calibrated using the known mass spectra. The time resolution is determined by the TDC, which for

Figure 2.23: *Photograph of the position sensitive detector and flange from the side. From top to bottom: mesh, MCP stack, delay-line anode, insulating ring, flange, and electrical feedthrough.*

the LeCroy3377 is 500ps.

Fig. 2.24 shows the backside of the detector, highlighting the helically wound delay lines which are used to determine the incident position of a charged particle. Each delay line consists of two wires with a fixed difference in length. One of the spirals is biased at +25 V with respect to the second. The 8 terminal points can be seen at the corners of the detector. The signals in each corner are combined as a twisted pair and attached to the electric feedthrough. These signals are amplified and discriminated before the time is determined by the TDC.

The encoding of the position is made in the following way: the localized cloud of electrons is accelerated from the back side of the MCP pair onto the helically wound wires. The electric pulse generated on the wires travels in opposite directions along each wire, as is shown schematically in Fig. 2.25 [Doo03]. The specifications quote that speed of propagation for the DLD-80 is 0.98 ns/mm. The time of propagation to reach each end of the wire is measured. The difference in arrival time between the two signal s is proportional to the position on the wires. The two wires must be orthogonally oriented to uniquely determine the spatial location of the incident charged particle (or photon).
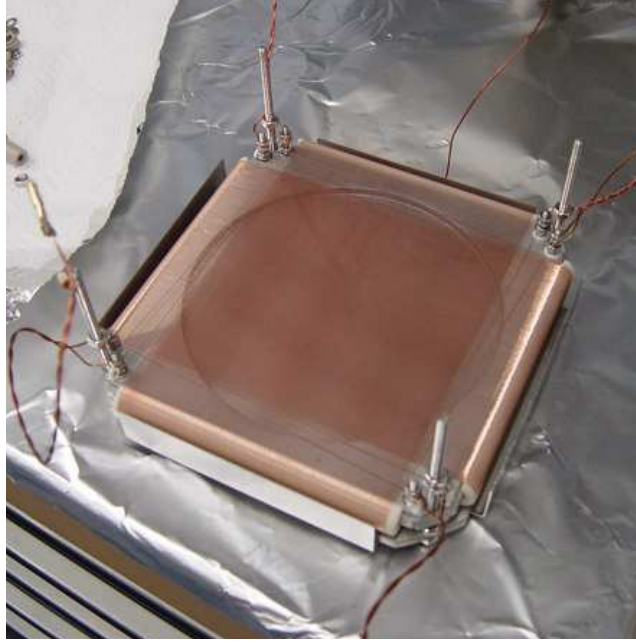
Figure 2.24: *A photograph of the backside of the delay line detector. The two sets of wires orthogonally oriented delay lines are seen. An incident electronic signal propagates along the wires to the corners, where the signal is taken, amplified, and measured.*

Each event has five coordinates: T, t_{x1}, t_{x2}, t_{y1}, t_{y2}. The time of flight, T, is recorded directly from the MCP signal. Each spatial axis has two time signals which are subtracted to give the position for that coordinate.

$$
\begin{aligned}
X &= t_{x1} - t_{x2} \\
Y &= t_{y1} - t_{y2}
\end{aligned}
\tag{2.26}
$$

Since the delay lines are dispersive, $t_{x1}+t_{x2} \approx t_{y1}+t_{y2}$. These numbers form the basis of the subsequent data analysis.

The spatial resolution for this arrangement is determined by the timing resolution of the TDC. The timing resolution is 0.5 ns which results in a spatial resolution of 0.03 mm. A further limitation of the resolution is the center-to-center distance of two neighboring MCP channels. The pore size for the MCP is approximately 25 μm.

The detector is capable of multiple hits (up to 16, determined by TDC) the dead time of the detector is on the order of 20ns. In principle, multiple events occurring simultaneously on the grid can be distinguished, since there is a fixed time difference between two signals on opposite ends of the wire.
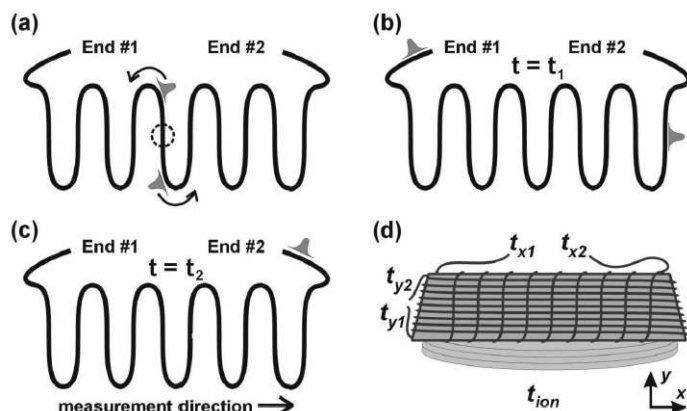
Figure 2.25: *The delay line principle. In picture a., an electron cloud is incident onto the delay line and an electrical signal propagates in each direction. In picture b. and c., the two pulses reach the end. The difference in time is proportional to the position. In picture d., two orthogonal delay lines are shown and are sufficient to determine the 2D position.*

The basic data acquisition program is provided by the company and is called CoboldPC. This provided the basic functions for reading the TDC and was used to develop a program to visualize the raw data by reconstructing the TOF spectrum and 2-D image.

Further analysis software has been self-developed separately with LabView. This software was developed to handle the raw 2D image (rotation) and extract information about the shape of the spatial distribution.

2.7   Reaction Microscope

The photoelectron spectra provide information about the ionization process. To be certain of the origin of the electron, it is necessary to measure the ion in coincidence. The "Reaction Microscope" is a combined position sensitive Photoion-photoelectron-coincidence (PEPICO) apparatus which allows kinematically complete measurements. Experiments were performed in collaboration with the group of Dr. Horst Rottke. A brief summary of the apparatus and the analysis associated with the detection of electrons will be presented here.

The measurement technique is based on the COLTRIMS method [UMD97]. The reaction microscope detector used in this work has been described in [MFS00] and a

simplified schematic is shown in Fig. 2.26. This work focused solely on the angular distribution of electrons in coincidence with C_{60}^+ or C_{60}^{2+}.
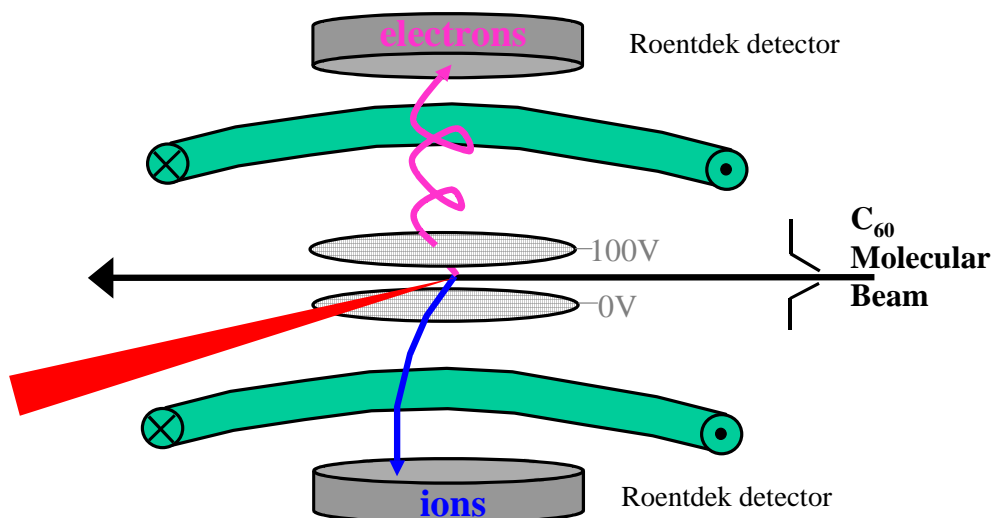

Figure 2.26: *Schematic of the "reaction microscope" apparatus. Both the ions and electrons are driven onto Roentdek delay line anodes to determine the temporal and spatial distributions. The ions and electrons are detected in coincidence.*

The laser beam is tightly focused onto the thin molecular beam, so that the molecules interact only at the focus with a Gaussian intensity distribution. To keep the count rate below one per 20 shots, the molecular beam density must be reduced. The C_{60} molecular beam was resistively heated to only 670 K in an effusive oven similar to the one described previously. After ionization, the electrons and ions are accelerated in opposite directions and are incident onto Roentdek delay-line detectors and the position and time are recorded for each particle. A homogeneous magnetic field of 1-2 mT was used to guide the electrons onto the detector.

The position of the electron was recorded as described previously. The raw measurement is the discrete intervals of time and position, Δt and $\Delta x, \Delta y$, respectively. From these quantities, the time-of-flight, as well as the momentum components of the electron parallel to the time of flight axis, p_e, and perpendicular, p_{xye}, can be determined.

The kinetic energy is then calculated by

$$E_{kin} = (p_e^2 + p_{xye}^2)/2m \tag{2.27}$$

and the polar angle, θ, can be calculated in radians by the relation

$$\theta = \arcsin\left(\frac{p_{xye}}{\sqrt{p_e^2 + p_{xye}^2}}\right) \tag{2.28}$$

In changing the distribution of the electrons from time and space to energy and angle, the proper Jacobians must be taken into consideration. The Jacobian between time and energy has been given by Eq. 2.25. The Jacobian between space and angle will now be considered.

The pixels of the detector have an equivalent area. The measurement can be considered as a solid angle with $\Delta\Omega = \Delta x \Delta y / L$, with L being the length of the time of flight[2]. In Fig. 2.27, the graph on the left shows the distribution of electron $f(E,\Omega)$ at an energy interval of 0.8 to 1.1 eV **before** applying the angular Jacobian[3].

To change the distribution to the case of constant $\Delta\theta$, the Jacobian is given by Eq. 2.29.

$$\Delta\Omega = \sin\theta\Delta\theta\Delta\phi \Rightarrow \Delta\theta = \frac{\Delta\Omega}{\sin\theta\Delta\phi} \tag{2.29}$$

Because of cylindrical symmetry, integration over ϕ always gives a constant value of 2π. Therefore, to convert the measured distribution to a distribution of constant θ, the following conversion is necessary.

$$f(E,\theta) = \frac{f(E,\Omega)}{2\pi\sin\theta} \tag{2.30}$$

This situation is equivalent to having a fixed detector of limited solid angle and rotating the polarization to build the angular dependence, which Hoffmann presented in his thesis [Hof00]. The right side of Fig. 2.27 shows the distribution **after** taking the angular Jacobian into account.

2.8   Time-Resolved Pump-Probe Spectroscopy

Time resolved pump-probe spectroscopy has become a standard method for monitoring the dynamics of a system. Femtosecond time resolution allows the observation of nuclear motion, short lived electronic states, formation of products, energy redistribution, and transient species. Pioneering experimental and conceptual work has been

---

[2]In reality, this is not so easy to picture since the electron is following a helical path, but nevertheless the principle idea is the same

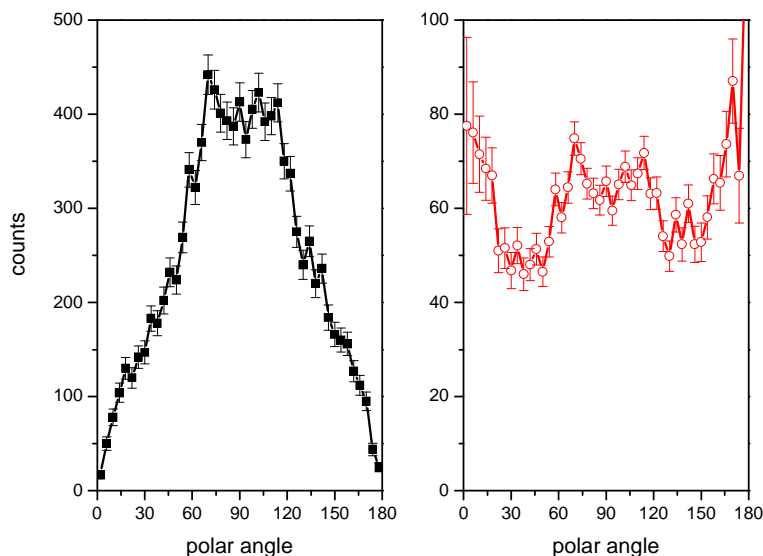[3]This is the distribution which was provided from the experimental analysis program.

Figure 2.27: *The left hand side shows the "raw" angular electron distribution provided by the experimental analysis program for electrons between 0.8 and 1.1 eV. To convert this distribution to that of constant polar angle, Eq. 2.30 has been applied and the resulting distribution is presented on the right hand side of the figure.*

made by Zewail , who received the 1999 Nobel prize for Chemistry. The "pump" pulse provides an initial excitation (a wave packet (if it is a coherent excitation), defined as a non-stationary, coherent superposition of molecular eigenstates) which evolves along a reaction coordinate until the "probe" pulse questions the state of the molecule at a defined time delay.

Experimentally, the pump-probe scheme can be achieved as shown in Fig. 2.28. This particular setup was used for the measurements with C_{60}. The laser pulses passed through a 100 μm BBO crystal, which has at best a 10% conversion efficiency. The output of the crystal contains both the fundamental and second harmonic, which are separated by a mirror which is highly reflective for 400nm and high transmission for 800nm.

The two pulses travel different pathways before being recombined. The 800 nm pulse can be arbitrarily delayed with respect to the 400 nm pulse by a delay stage (Physik Instrumente - DG300). Since the focal length is wavelength dependent (this is due to the wavelength dependence of the index of refraction), the 400 nm pulse traversed a negative lens of -2 diopters, making the 400 nm beam divergent and increasing the focal length to roughly match that of the 800nm.
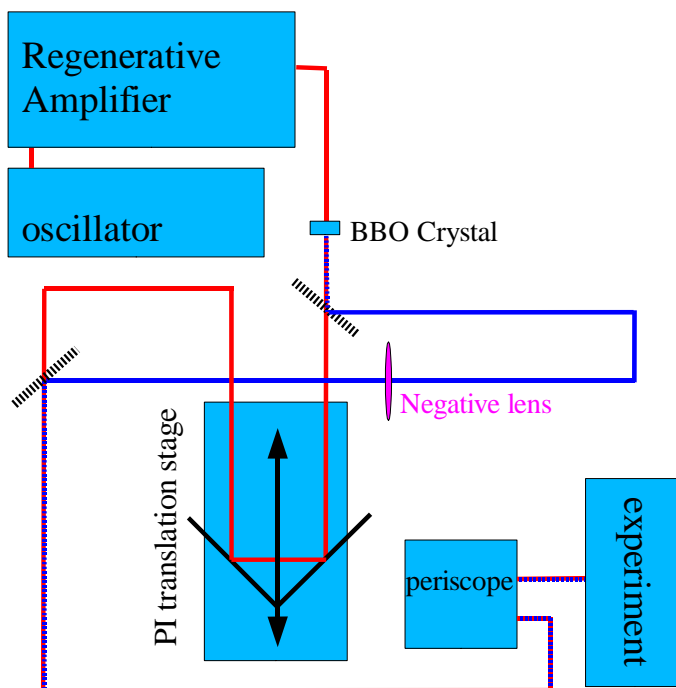
Figure 2.28: *Simplified diagram of the two-color pump-probe setup. The second harmonic is generated in a BBO crystal. The two colors are separated by a highly reflective mirror for 400nm (with high transmission for 800nm). Temporal overlap was found by producing the third harmonic in a BBO crystal.*

2.9   Femtosecond Pulse Manipulation

The control of molecular processes by manipulation of the phase and amplitude of the laser pulse electric field has been a hot topic of recent research. Development of femtosecond laser sources and programmable liquid crystal (and acousto-optical) modulators are the basis of the recent explosion in research in this direction. This work applies the pulse shaping technique and a closed loop optimization program to control the fragmentation of C_{60}. The liquid crystal modulator(LCM) pulse shaping apparatus and implementation is described in this chapter. Finally, global optimization algorithms will be discussed.

2.9.1   Femtosecond Laser Pulse Shaping

The temporal form of a femtosecond pulse can be altered in the frequency domain by phase masks. Prior to the 1980s (for ps laser pulses), modulation was achieved by fixed phase masks [DGo71], consisting of variable thickness transparent media substrates. By 1990, Weiner and colleagues had developed a computer controlled LCM, which can vary the phase pattern [PWL90]. LCMs have become one cornerstone of the recent drive for control of molecules.

A full description of an LCM device and its operation can be found in [Wei00] or [Boy00]. The latter describes the first shaping device (CRI-SLM256) implemented at the Max Born Institute. The present work was done with a single array, 640 Pixel LCM from Jenoptik (SLM-640) [SHF01]. There are several differences between the two spatial light modulators (SLMs) and their implementation.

The Jenoptik pulse shaper was chosen because of its large active window. The array is composed of 640 pixels, where each pixel is 97 μm wide, 7 mm tall, and 9μm thick. A 3 μm gap is present between adjacent pixels. The larger window allows pulse energies of up to 500μJ to be incident onto the shaper without surpassing the damage threshold. To stay below the damage threshold, the beam was kept as large as possible. Assuming a 500μJ, 30 fs pulse is incident onto the liquid crystals with a spot size equal to the active area (63.7 mm x 7 mm = 445.9 mm^2), the peak intensity is found to be $\sim$ 4 GW / cm^2. This is well below the quoted damage threshold of 300 GW/cm^2. A schematic representation of the pixel array is shown in Fig. 2.29.

The liquid crystal array was placed at the Fourier plane of an all reflective "4-f zero dispersion stretcher", as shown in Fig. 2.30. A 4-f (four times the mirror/lens focal length) zero dispersion stretcher is a device which maps frequency to space, i.e., a spatial distribution of frequency components, before spatially recombining the frequency components. Alignment is made so that the optical path length of every wavelength component is equivalent, and does not give rise to temporal dispersion/chirp. The incident laser irradiation is spectrally dispersed using a 1800 line/mm holographic grating (Spectrogon). The first order diffraction is sent to a plane mirror, which guides the radiation to a dielectric coated cylindrical mirror with focal length $f = 40$ mm. The cylindrical mirror focuses the individual wavelength components horizontally but not vertically onto the LCM. At this point (two times the focal length, 2-f), the radiation is at the Fourier plane. The laser pulse then traverses the "opposite" manner, and is spatially refocussed.

The crystals are rod-like molecules which align under mechanical or electrical
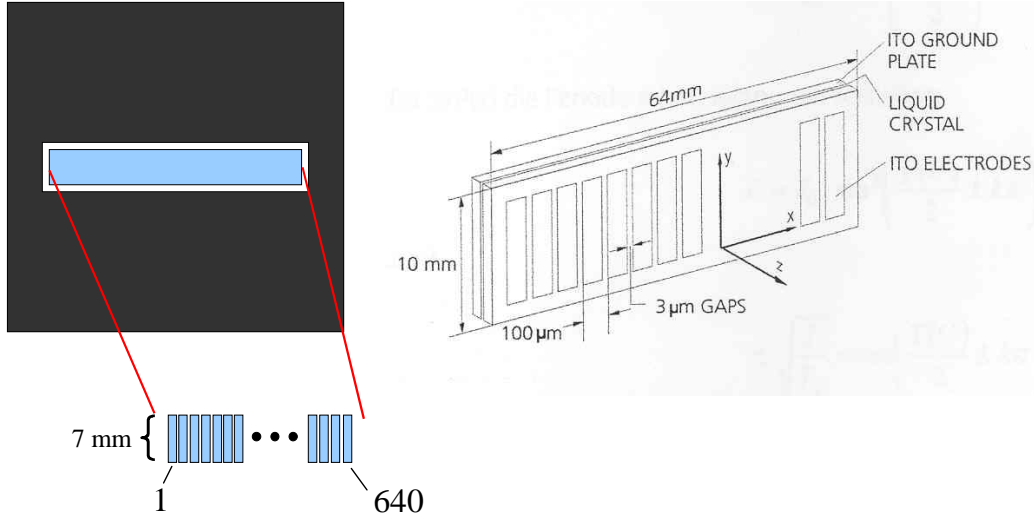
Liquid Crystal Modulator

Figure 2.29: *A schematic of the liquid crystal array for a 640 pixel Jenoptik LCM. On the left is presented a front view of the LCM device On the right, an expanded view of active area of the LCM is shown.*

stress. The liquid crystals are a birefringent medium, which means the ordinary and extraordinary electric field waves have different optical path lengths. The optical path length difference is given by

$$\Lambda = d(|n_o - n_e|) \tag{2.31}$$

where d is the thickness of the crystal, n_o and n_e are the ordinary and extraordinary waves, respectively. The fast axis of the liquid crystals are parallel to the laser polarization, which is horizontally parallel to x in Fig. 2.29. By applying a voltage across the liquid crystal cell, an electric dipole is created on the molecules, due to their anisotropic dielectric properties. The lowest energy configuration is when they are aligned with the electric field. Molecules not aligned experience a torque, which forces them to align with the electric field. The rotation is made in the z direction. A cross-section of a liquid crystal is shown in Fig. 2.31.

By applying a voltage to transparent ITO (Indium Tin Oxide) electrodes, which coat the inner side of the glass plates defining the pixel, the crystals are rotated and the birefringence is modified. The rotation of the crystals causes the extraordinary index of refraction to alter, while the ordinary index of refraction remains constant. This electrically variable birefringence changes the optical path length which in turn
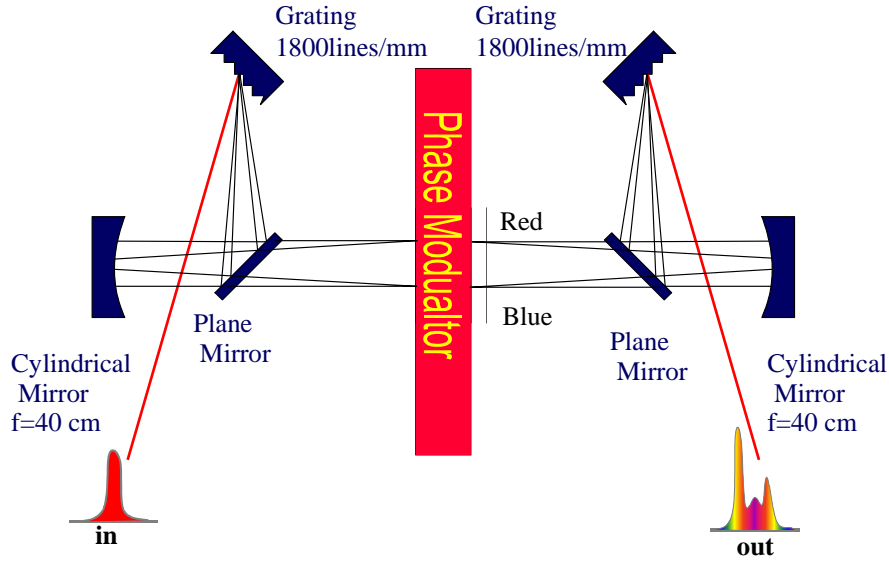
Figure 2.30: *Schematic of a 4-f zero dispersion stretcher with a liquid crystal modulator placed at the frequency Fourier plane. Changing the retardance for different frequency components results in a temporal modulation of the pulse shape.*

changes the phase difference. There is 12 bit control of the pixels which means there are 4096 voltage settings, commonly referred to as "drive values". The applied voltage varies between 0 V and 8 V. Many of these settings are superfluous since only 2π phase control is needed, and at 800 nm there is approximately 7π phase available over the complete voltage range. The phase difference, or retardance, can be written as

$$\Delta\phi_n = k\Lambda = \frac{2\pi d\Delta n(V)}{\lambda_n} \qquad (2.32)$$

where k is the wavevector, Λ is the optical path length difference $d(|n_o - n_e|)$ with d the thickness of the material, n_o and n_e are the ordinary and extraordinary index of refraction, respectively, and λ_n is the incident wavelength on pixel n.

Since there is only one array, either amplitude or phase shaping, could be performed, but not both simultaneously. Phase-only shaping was exclusively used in this work.

The frequencies are spread across the array by the gratings so that each pixel has a certain bandwidth per pixel incident upon it. The present configuration has been measured to be $\Delta\lambda = 0.17$ nm per pixel.
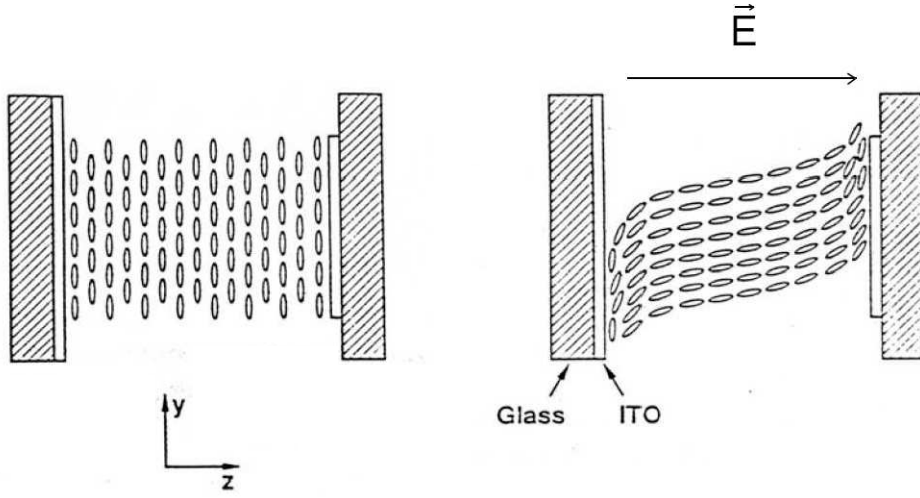
Figure 2.31: *Orientation of liquid crystals without (left) and with (right) applied electric field.*

Brief Theoretical Background to Pulse Shaping

An electric field can be considered in either the time or frequency domain, and the two domains are related to each other by a Fourier transform. The temporal modulation by LCMs of femtosecond pulses takes place in the frequency domain and can be considered as a linear filtering of the input signal. In the frequency domain, the output of a linear filter is the product of the input and the frequency response, $H(\omega)$.

$$\widetilde{E}_{out}(\omega) = H(\omega) \cdot \widetilde{E}_{in}(\omega) \tag{2.33}$$

where $\widetilde{E}_{out}(\omega)$ and $\widetilde{E}_{in}(\omega)$ are the complex electric fields outgoing and incoming from a linear filter, respectively. The frequency response can be written as

$$H(\omega) = R(\omega)e^{-i\Phi(\omega)} \tag{2.34}$$

where $R(\omega)$ represents the amplitude filter and $\Phi(\omega)$ is the phase factor. If a constant amplitude transmittance is selected, the outgoing electric field has the form

$$\widetilde{\mathcal{E}}_{out}(\omega) = Re^{-i\Phi(\omega)} \cdot \widetilde{\mathcal{E}}_{in}(\omega) \tag{2.35}$$

The temporal shape of the pulse can be found by taking the Fourier transform of $\mathcal{E}_{out}(\omega)$.

$$\widetilde{\mathcal{E}}_{out}(t) = \frac{R}{2\pi} \int_{-\infty}^{\infty} \widetilde{\mathcal{E}}_{in}(\omega)e^{-i\Phi(\omega)}e^{-i\omega_0 t}d\omega \tag{2.36}$$

where the term $e^{-i\omega_0 t}$ is a constant phase offset. In one simple example, $\Phi(\omega)$ can be written as the Taylor expansion about a central frequency ω_0

$$\Phi(\omega) = b_0 + b_1 (\omega - \omega_0) + \frac{1}{2} b_2 (\omega - \omega_0)^2 + \cdots \qquad (2.37)$$

where b_0 is a constant determining the relative temporal phase, $b_1 = \frac{d\Phi(\omega)}{d\omega}|\omega_0$ results in a linear chirp of frequencies (in time domain a change in position), and $b_2 = \frac{d^2\Phi(\omega)}{d\omega}^2|\omega_0$ provides a quadratic chirp, which can elongate or compress (if not bandwidth limited) a pulse.

The frequency response, $H(\omega)$, is related to the effective mask on the shaper, $M_{eff}(\omega)$, by the relation [Wei00],

$$H(\omega) = M_{eff}(\omega) = \int dx M(x) g(x, \omega) \qquad (2.38)$$

where the effective mask is given by the convolution of the physical mask, $M(x)$, and spatial intensity profile of the incident laser pulse $g(x, \omega)$.

2.9.2 Global Optimization Algorithms

Control of photo-molecular processes can be achieved by modulation of the electric field. By allowing certain frequencies to interact with a target at determined times or controlling the temporal input of energy to the molecule, certain pathways can be either enhanced or suppressed. In principle, when the potential energy surface of the target is well-known, an optimal pulse form can be directly calculated. In practice, all but the simplest molecules are practically impossible to calculate. By incorporating an adaptive learning feedback loop with the pulse shaping technique, the potential energy surface can be scanned without prior knowledge of the potential surfaces for a global minimum/maximum. Several systems of various complexity have been used as targets for optimization [ABB98, BDN01, HMM00, DFG03, SBT02].

Several global optimization algorithms exist to find the global maximum, among these are the simplex downhill, simulated annealing, and genetic algorithms. The optimization done in this work was performed with an evolutionary algorithm, a type of genetic algorithm. The program has been developed in LabVIEW.

A schematic of an optimization loop is illustrated in 2.32. The computer generates phase masks which are applied to the JenOptik LCM, which is at the center of a
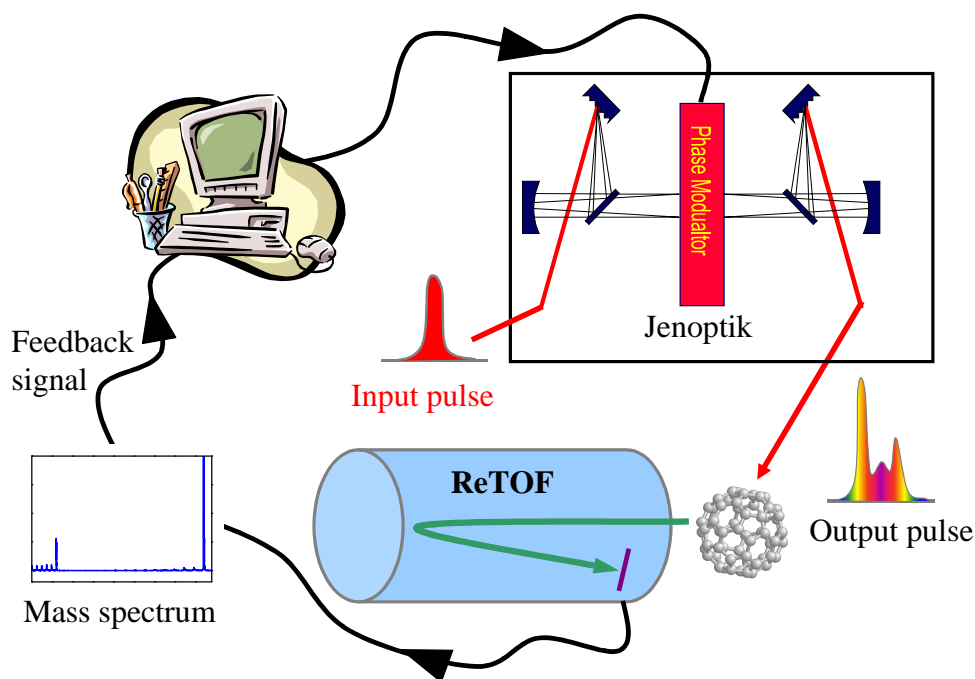
Figure 2.32: *Schematic of an adaptive optimization feedback loop. A self-learning algorithm, is used to analyze the feedback signal from the mass spectrum and generate new temporal pulse shapes.*

4-f zero dispersion stretcher. The output pulse from the stretcher, a temporally-modulated pulse, interacts with the molecular beam and ionizes and fragments the C_{60} molecules. Detection of the ions is made with the ReTOF. By analyzing the resulting mass spectra, new test pulse(s) are generated.

Genetic Algorithms are based loosely on evolutionary biology and many terms result from this concept. The important terms are given in Table 2.6.

The program begins with the creation of many individuals which constitute a population. The genes which encode the individual (and define the solution space) are generated completely at random. The individuals are applied separately to the pulse shaper and tested. A test consists of 3000 interaction events with the molecular beam and measurement of the resulting mass spectra. After every individual has been tested, a ranking is made based on the fitness function, which gives the interpretation of the "goodness" or "badness" of the individual. To generate the next generation, first, a number of the worst individuals are eliminated from the population. Next, the creation of the new generation is performed. Several (three) of the highest ranking individuals are passed directly to the next generation without alteration. This process

Table 2.6: *The important evolutionary terms and their significance in terms of an evolutionary algorithm using a liquid crystal modulator pulse shaper.*

Term	Definition in terms of pulse shaping
Individual	one trial pulse shape
Population	sum of individuals
Generation	one iteration of the evolutionary optimization loop
Gene	characteristic of individuals, one pixel, coefficient
Cross-over	interchanging genes between two individuals
Mutation	random change of 1 gene
fitness function	evaluation method

is termed "survival of the fittest". The remaining individuals undergo cross-over and mutation. These two processes are used to introduce new individuals into the population. In cross-over, two individuals are selected at random. Their genes are interchanged randomly. It is possible no genes are changed or one individual is erased. Mutation is performed by random change of one gene. The gene or genes which are mutated are selected at random. Many genes per individual could be changed or none at all.

The new population is then tested and ranked, and this continues until the stopping criterion is reached. The algorithm is non-deterministic, meaning the pathway to the optimum is not defined.

Efficient running of the optimization loop is not straight forward, but the algorithm is fairly robust. The speed of convergence depends on the number of free parameters, as well as the difficulty of the problem. Typically, it is useful to parameterize the solution space to be searched. For example, if one wants to compress a chirped pulse, one can reduce the search space by using only the coefficients of the Taylor expansion of phase.

For the optimization of fragmentation, the number of free parameters was reduced by grouping n adjacent pixels together. The group of n pixels functioned as one pixel. This reduces the active pulse shaping window (maximal time window is proportional to $\delta\omega$). In the present setup, a grouping of pixels by 4 results in a maximum time window of $\sim$3ps. This window is sufficient for the processes expected for C_{60}.
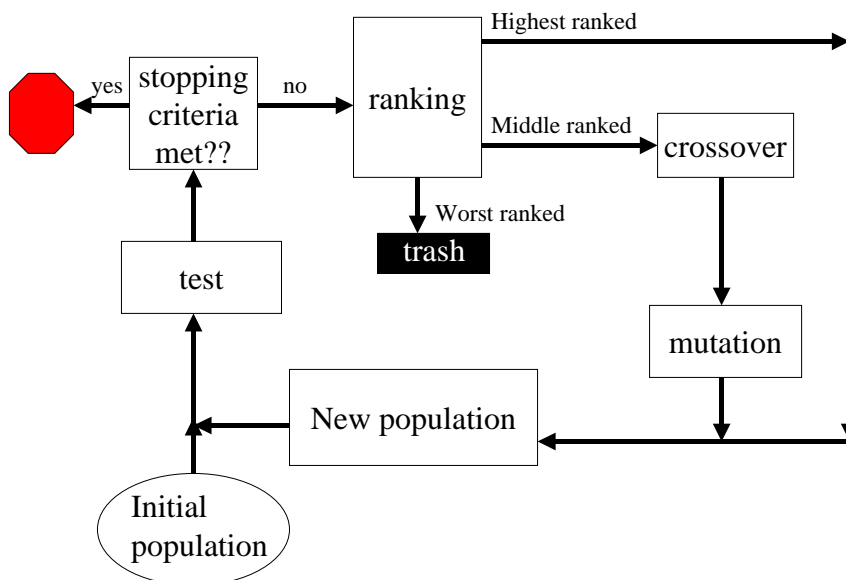
Figure 2.33: *A block diagram of the evolutionary algorithm loop implemented in this work.*